J. Fluid Mech. (2011), *vol.* 678, *pp.* 317–347.
doi:10.1017/jfm.2011.114

Hydrodynamic stability and breakdown of the viscous regime over riblets

RICARDO GARCÍA-MAYORAL† AND JAVIER JIMÉNEZ
School of Aeronautics, Universidad Politécnica de Madrid, 28040 Madrid, Spain

(Received 12 July 2010; revised 1 February 2011; accepted 3 March 2011;
first published online 19 April 2011)

The interaction of the overlying turbulent flow with a riblet surface and its impact on drag reduction are analysed. The 'viscous regime' of vanishing riblet spacing, in which the drag reduction produced by the riblets is proportional to their size, is reasonably well understood, but this paper focuses on the behaviour for spacings $s^+ \simeq 10$–20, expressed in wall units, where the viscous regime breaks down and the reduction eventually becomes an increase. Experimental evidence suggests that the two regimes are largely independent, and, based on a re-evaluation of existing data, it is shown that the optimal rib size is collapsed best by the square root of the groove cross-section, $\ell_g^+ = A_g^{+1/2}$. The mechanism of the breakdown is investigated by systematic DNSs with increasing riblet sizes. It is found that the breakdown is caused by the appearance of long spanwise rollers below $y^+ \approx 20$, with typical streamwise wavelengths $\lambda_x^+ \approx 150$, that develop from a two-dimensional Kelvin–Helmholtz-like instability of the mean streamwise flow, similar to those over plant canopies and porous surfaces. They account for the drag breakdown, both qualitatively and quantitatively. It is shown that a simplified linear instability model explains the scaling of the breakdown spacing with ℓ_g^+.

Key words: drag reduction, turbulent boundary layers, turbulence control

1. Introduction

The reduction of skin friction in turbulent flows has been an active area of research for several decades, and surface riblets have been one of the few drag-reduction techniques successfully demonstrated not only in theory, but in practice as well. They are small protrusions aligned with the direction of the flow that confer an anisotropic roughness to the surface. The most comprehensive compilations of riblet experiments are those of Walsh & Lindemann (1984), Walsh (1990*b*), Bruse *et al.* (1993) and Bechert *et al.* (1997), in which the maximum drag reductions are of the order of 10 %, and are achieved for riblets with peak-to-peak spacings of approximately 15 wall units.

The dependence of the performance of riblets with a particular geometry in terms of the rib spacing is sketched in figure 1. In the limit of very small riblets, which we will call the 'viscous' regime, the reduction in drag is proportional to the riblet size, and its mechanism is fairly well understood and quantified (Bechert & Bartenwerfer 1989; Luchini, Manzo & Pozzi 1991). However, as the riblets get larger and their effect saturates, a minimum drag is reached when the viscous regime 'breaks down'. We will see below that the two regimes are only weakly related, and that the breakdown is

† Email address for correspondence: ricardo@torroja.dmt.upm.es

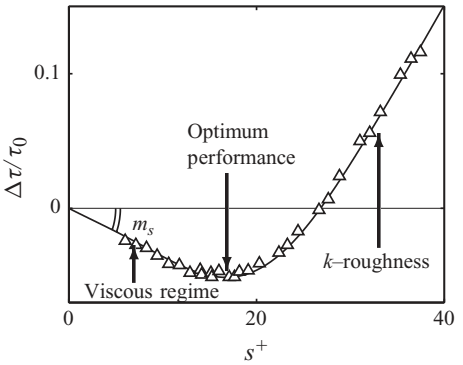

FIGURE 1. Effect of the peak-to-peak distance, s^+, on the skin friction of a triangular riblet with 60° peak sharpness, from Bechert *et al.* (1997).

worse understood than the viscous limit, in spite of having been the subject of several studies (Choi, Moin & Kim 1993; Goldstein & Tuan 1998). The main focus of our paper is to determine the parameters that best describe the extent of the linear regime and the mechanism that controls the breakdown. Apart from the theoretical interest, a practical reason is that the breakdown spacing limits the optimum performance of a given riblet geometry, which can roughly be estimated as the product of the viscous slope and the breakdown size. In particular, if it could be clarified how the latter is related to the geometry of the riblets, it might be possible to design surfaces with larger critical sizes than the ones available at present, and consequently with better peak performances.

The paper is organized in two parts. The first one summarizes the available experiments and theoretical understanding. Within this part, § 2 reviews the different drag-reduction regimes and discusses the physical mechanisms proposed in the literature both for the viscous regime and for its breakdown, and § 3 discusses the suitability of the parameters traditionally used to characterize the latter and proposes an empirical alternative. The second part of the paper addresses the mechanism of the breakdown, using direct numerical simulations (DNSs). Section 4 outlines the numerical method and the parameters of the simulations. The results are presented in § 5, which also discusses the relationship between the breakdown, the riblet size and the overlying turbulent flow, and § 6 proposes a linear stability model that captures the essential attributes of the breakdown, including an approximate justification of the scaling parameter proposed in § 3. The conclusions are summarized in the final section.

2. Drag-reduction regimes for riblets

2.1. *The viscous regime*

Early in the investigation of riblets, Walsh & Lindemann (1984) showed that the Reynolds number dependence of the effect of a given riblet geometry on the skin friction could be approximately expressed in terms of the riblet spacing measured in wall units, $s^+ = su_\tau/\nu$, where ν is the kinematic viscosity, and $u_\tau = \sqrt{\tau_w}$ is the friction velocity defined in terms of the kinematic skin friction τ_w. Throughout this paper the fluid density will be taken as constant and equal to unity. Figure 1 shows a typical curve of drag reduction as a function of the riblet spacing. In the viscous regime, for small s^+, the contribution of the nonlinear terms to the interaction of the flow with the riblets is negligible and, if τ_{w0} is the skin friction for a smooth wall, the drag

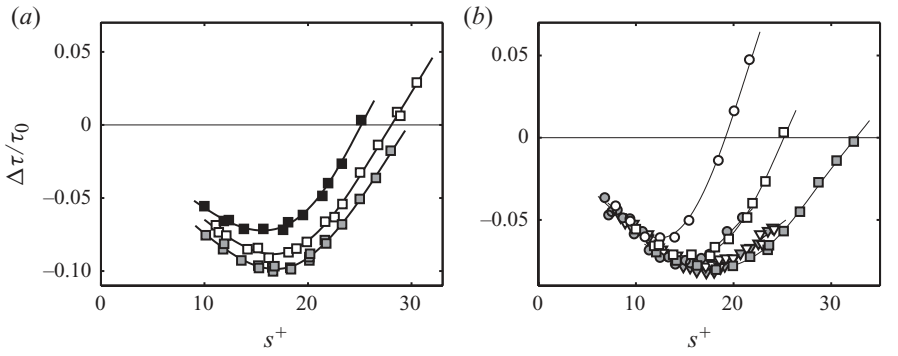

FIGURE 2. Drag reduction curves of various riblets, adapted from Bechert *et al.* (1997). (*a*) Blades with fixed height-to-spacing ratio, $h/s = 0.5$, and different tip width, t/s. Solid symbols, $t/s = 0.04$; open symbols, $t/s = 0.01$; grey, $t/s = 0.02$ with improved blade alignment and groove impermeability. (*b*) Riblets with approximately equal viscous slope m_s. ■, blades with $h/s = 0.4$ and $t/s = 0.01$; □, blades with $h/s = 0.5$ and $t/s = 0.04$; ●, scalloped groves with $h/s = 0.7$ and $t/s = 0.015$; ○, scalloped groves with $h/s = 1.0$ and $t/s = 0.018$; ▼, trapezoidal riblets with tip angle 30°; ▽, trapezoidal riblets, 45°.

reduction $DR = -\Delta\tau_w/\tau_{w0}$ depends linearly on s^+. That regime eventually breaks down, and the drag reduction is typically maximum for spacings $s^+_{opt} \approx 10$—20. For even larger riblets, the reduction ultimately becomes a drag increase and follows a typical k-roughness behaviour (Jiménez 2004). The parameters that determine the optimum performance of a given riblet are s^+_{opt} and the slope of the drag curve in the viscous regime:

$$m_s = -\left.\frac{\partial(\Delta\tau_w/\tau_{w0})}{\partial s^+}\right|_{s=0} = -\left.\frac{\Delta\tau_w/\tau_{w0}}{s^+}\right|_{s^+\ll 1}. \tag{2.1}$$

Both depend on the geometry, but the qualitative behaviour is always as just described.

The analysis of the available experimental evidence suggests that the viscous and breakdown regimes are essentially unrelated phenomena. For example, blade thickness has a strong effect on the viscous performance of thin-blade riblets without appreciably changing their groove geometry, and figure 2(*a*) shows an example of progressively thicker blades (1–4 %), with fairly different viscous slopes and very similar breakdown spacings. Conversely, figure 2(*b*) is a compilation of drag curves for riblets with similar m_s but different geometries, whose optimum spacings vary widely. To separate the two effects as much as possible, and to focus on the breakdown mechanism, most of our discussion from now on will use drag curves normalized so that their initial viscous slopes are unity.

It is widely believed that the drag-reduction properties of riblets in the viscous regime are well described by the concept of 'protrusion height', which was initially introduced by Bechert & Bartenwerfer (1989) as an offset between the virtual origin seen by the mean streamwise flow and some notional mean surface location. The correct form was given by Luchini *et al.* (1991), who defined it as the offset between the virtual origins of the streamwise and spanwise flows. From here on, we will denote the streamwise, wall-normal and spanwise coordinates by x, y and z, respectively, and the corresponding velocity components by u, v and w. The origin for y will be taken at the top of the riblet tips.

There is a thin near-wall region in turbulent flows over smooth walls where viscous effects are dominant, nonlinear inertial effects can be neglected and the mean velocity

profile is linear. Its thickness is 5–10 wall units (Tennekes & Lumley 1972). From the point of view of a small protrusion in this layer, the outer flow can be represented as a time-dependent but otherwise uniform shear. Riblets destroy that uniformity near the wall but, if $s^+ \ll 1$, the flow still behaves as a uniform shear for $y \gg s$. A further simplification is that the problem decouples into two two-dimensional sub-problems in the z–y cross-plane, because the equations of motion are locally linear, the riblets are uniform in the streamwise direction and the shear varies only slowly with x when compared to its variations in the cross-plane. The first sub-problem is the longitudinal flow of u, driven by a streamwise shear that takes the form

$$u \approx S_x(x,t)\,(y - \Delta_u) \tag{2.2}$$

at $y^+ \gg 1$, and the other is the transverse flow of v and w, driven by

$$w \approx S_z(x,t)\,(y - \Delta_w) \quad \text{and} \quad v \approx 0. \tag{2.3}$$

Far from the wall, the effect of the riblets reduces to the virtual origins Δ_u and Δ_w (Luchini 1995), which are different for the two flow directions. What Luchini *et al.* (1991) suggested was that the 'protrusion height' between the two virtual origins, $\Delta h = \Delta_w - \Delta_u$, was the controlling parameter for the viscous drag reduction. Intuitively, if the virtual origin for the crossflow is farther into the flow than the one for the longitudinal one ($\Delta h > 0$), the spanwise flow induced by the overlying streamwise vortices is impeded more severely than over a smooth wall. The vortices are displaced away from the wall, and the turbulent mixing of streamwise momentum is reduced. Since this mixing is responsible for the high local wall shear (Orlandi & Jiménez 1994), the result is a lower skin friction. This was verified by Jiménez (1994) by DNSs in which Δh was introduced independently of the presence of riblets.

The numerical calculation of Δh only requires the solution of the two stationary two-dimensional Stokes problems for Δ_u and Δ_w, which are computationally much less intensive than the three-dimensional, time-dependent, turbulent flow over ribbed walls. Note that the linearity of the Stokes problems implies that Δ_u, Δ_w and Δh are all proportional to the riblet size in the viscous regime, as observed in experiments.

2.2. *The breakdown of the viscous regime*

As s^+ increases, the predictions of the viscous theory break down, particularly the linear dependence on s of the drag. The theories proposed in the literature for this deterioration of performance fall in two broad groups, both of which focus on the behaviour of the crossflow.

The first one is that the riblets lose effectiveness once s^+, which is used as a measure of the Reynolds number of the crossflow, increases beyond the Stokes regime. For example, Goldstein & Tuan (1998) suggested that the deterioration is due to the generation of secondary streamwise vorticity over the riblets, as the unsteady crossflow separates and sheds small-scale vortices that create extra dissipation. However, it is known that spanwise oscillations of the wall, which also presumably introduce unsteady streamwise vorticity, can decrease drag (Jung, Mangiavacchi & Akhavan 1992), and that modifying the spanwise boundary condition to inhibit the creation of secondary wall vorticity increases drag (Jiménez 1992; Jiménez & Pinelli 1999). Both observations suggest that introducing small-scale streamwise vorticity near the wall decreases drag by damping the larger streamwise vortices of the buffer layer, and that inertial crossflow effects need not be detrimental to drag reduction.

A related possibility that was considered during the course of the present study was that the concept of protrusion height could be extended beyond the strictly viscous

regime, and that the observed deviations from linearity would be due to the increased importance of advection in the vicinity of the riblets. In that model, the flow far from the riblets would still be a uniform shear but within the riblets, it would begin to feel the effects of the finite Reynolds number. If that were the case, the breakdown could still be estimated from simple two-dimensional calculations analogous to the viscous ones. Unfortunately, simulations based on that model (García-Mayoral & Jiménez 2007) resulted only in small departures from the viscous values, of variable sign depending on the riblet geometry and size. Changes of the order required to explain the experiments were not reached until $s^+ \approx 20$–40, which is too large compared to $s^+ \approx 10$–20 found experimentally.

The second group of theories assumes that the observed optimum spacing is related to the scale of the turbulent structures in the unperturbed turbulent wall region. In that group we could mention the observations by Choi *et al.* (1993), Suzuki & Kasagi (1994) and Lee & Lee (2001), that the streamwise turbulent vortices lodge within the riblet grooves for riblets in the early drag-degradation regime.

All those models result in optimum spacings of roughly the right order of magnitude, but they can be characterized as 'circumstantial' in the sense that they are based on observations at spacings for which the viscous regime has already broken down, rather than at those preceding the deterioration. Moreover, although they suggest plausible reasons for why the Stokes regime fails beyond a certain riblet size, none of them provides convincing physical arguments for why that failure should lead to a drag increase. As a consequence, it is difficult to establish with certainty whether the observed phenomena are consequences or causes of the breakdown, and the ultimate reason for the observed degradation of the effectiveness of riblets can still be considered as open.

3. Scaling of the riblet dimension at breakdown

As already mentioned, one of the earliest observations concerning riblets was that the drag-reduction curves for a given riblet geometry could be described in terms of the riblet size expressed in wall units. Size has often been taken to mean the spacing s^+, although occasionally the depth h^+ has also been used. For a particular geometry, both quantities are proportional to each other, and the choice is immaterial, but the same is not true when comparing riblets of different shapes, and we saw in figure 2 that s^+ is not, in that sense, a particularly good characterization of the position of the viscous breakdown.

In this section, we attempt to determine empirically which geometrical characterization of the riblet best collapses the critical breakdown size across different riblet shapes. Figure 3(*a*) illustrates the variation of s^+_{opt} from one geometry to another. The figure portrays the optimum spacing for several experimental riblets against the ratio of the groove cross-section to the square of the spacing, A_g/s^2, which is a measure of their depth-to-width ratio. Although s^+_{opt} is always in the range 10–20 mentioned above, it is clear that deeper grooves break down earlier and achieve their optimum performance for narrower spacings. Note that this effect cannot be explained by any of the breakdown models discussed in § 2.2. For example, the lodging of buffer layer vortices within the riblet grooves might qualitatively explain why the drag reduction breaks down for riblet spacings of the order of the vortex diameters, about 20 wall units according to Kim, Moin & Moser (1987), but it does not explain why the groove depth affects s^+_{opt}.

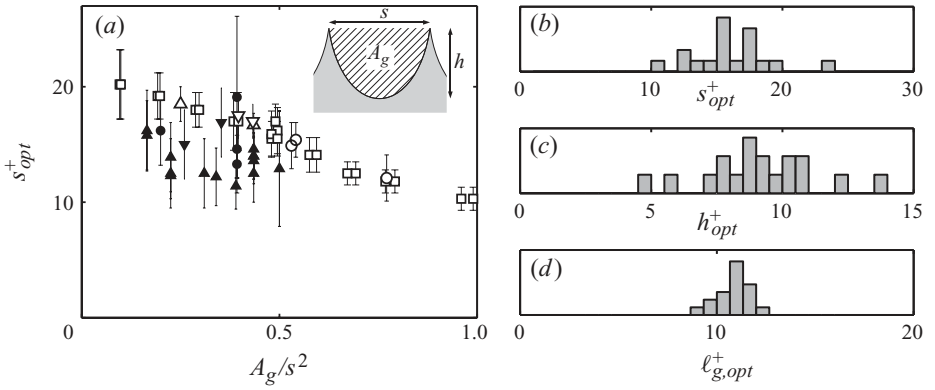

FIGURE 3. (*a*) Riblet spacing for maximum drag reduction, as a function of the relative groove cross-section A_g/s^2. △, triangular riblets; ▽, notched-top and flat-valley riblets; ○, scalloped semicircular grooves; □, blades. The solid symbols are from Walsh & Lindemann (1984) and Walsh (1990*b*), and the open symbols are from Bechert *et al.* (1997). Error bars have been estimated from the drag measurement errors given in the references. (*b–d*) Histograms of the optimum performance point, expressed in terms of the peak-to-peak spacing s, the groove depth h and the square root of the groove cross-section, $\ell_g = \sqrt{A_g}$, for several riblet geometries.

A non-exhaustive search among possible definitions of riblet size gave as a result that the best collapse of breakdown dimensions was achieved in terms of the groove cross-section, $\ell_g^+ = (A_g^+)^{1/2}$. We portray in figures 3(*b*)–3(*d*) the histograms of the breakdown dimensions of several riblets, expressed as s^+, h^+ and ℓ_g^+. We have omitted experiments for which the optimum performance could not be clearly defined, such as the measurements for fibres of Bruse *et al.* (1993), or those for seal fur of Itoh *et al.* (2006). Disregarding them, the histograms show that the optimum values of s^+ and h^+ have scatters of the order of 40 %, while the scatter for ℓ_g^+ is only about 10 %. The implied optimum is $\ell^+_{g,opt} \simeq 10.7 \pm 1$.

Scaling the whole drag-reduction curves requires both normalizing the riblet size with ℓ_g^+ and scaling the drag reduction with the new viscous slope m_ℓ,

$$m_\ell = -\left.\frac{\Delta\tau_w/\tau_{w0}}{\ell_g^+}\right|_{\ell_g^+\ll 1} = \frac{s}{\ell_g} m_s, \tag{3.1}$$

so that $DR = m_\ell \ell_g^+$ in the viscous regime, with the implication that DR/m_ℓ should be a 'universal' function of ℓ_g^+.

The slope m_ℓ is a viscous quantity that can be obtained from Stokes two-dimensional calculations. According to the classical theory of wall turbulence, surface manipulations only modify the intercept of the logarithmic velocity profile by an amount ΔB (Clauser 1956), which in turn changes the free-stream velocity, U_δ^+, and the friction coefficient $c_f = 2\tau_w/U_\delta^2 = 2/{U_\delta^+}^2$. The drag reduction can then be expressed as (Jiménez 2004; García-Mayoral & Jiménez 2011)

$$\frac{\Delta c_f}{c_{f0}} \approx \frac{\Delta\tau_w}{\tau_{w0}} \approx \frac{-\Delta B}{(2c_{f0})^{-1/2} + (2\kappa)^{-1}}, \tag{3.2}$$

where $\kappa \approx 0.4$ is the von Kármán constant. If ΔB is positive, the logarithmic profile is shifted 'upwards' and friction is reduced, and *vice versa*. For riblets in the viscous regime, the shift is proportional to the protrusion height, $\Delta B = \mu_0 \Delta h^+$, with a

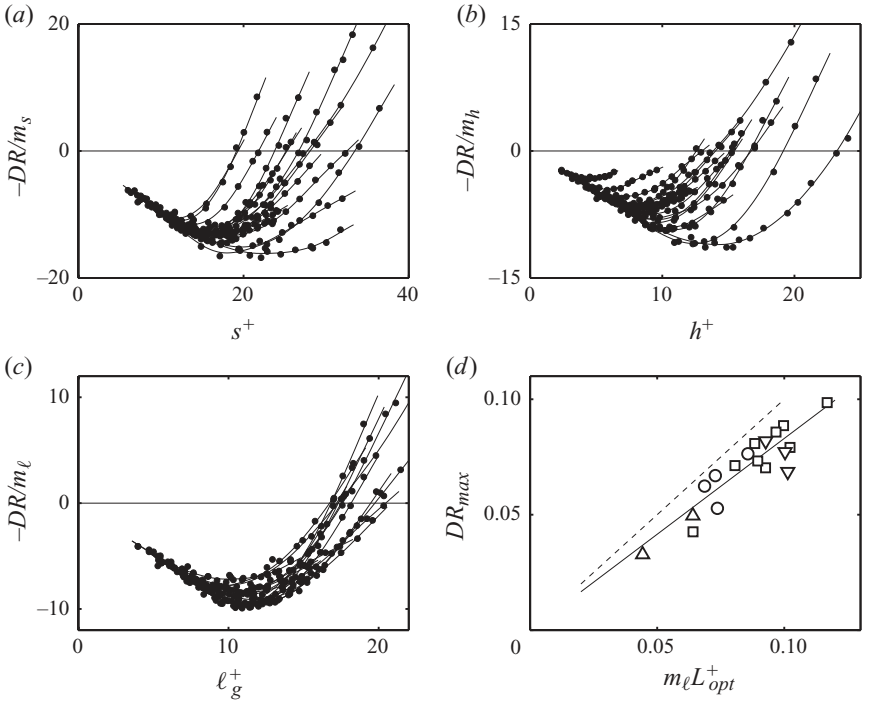

FIGURE 4. Drag-reduction curves from Bechert *et al.* (1997), reduced to a common viscous slope, as functions of (*a*) s^+, (*b*) h^+ and (*c*) ℓ_g^+. (*d*) Maximum drag reduction compared with the prediction obtained by estimating $\ell^+_{g,opt} = 10.7$. The symbols are the same as in figure 3; – – – –, linear extrapolation from the viscous regime; ——, linear fit with slope 0.83.

proportionality constant that has been estimated as $\mu_0 \approx 0.66$ (Jiménez 1994) or $\mu_0 \approx 0.785$ (Bechert *et al.* 1997), although the two values are too similar to be distinguished experimentally. The above considerations can be combined in an expression for the viscous slope that only depends on the Stokes calculation of the protrusion height,

$$m_\ell = \frac{\mu_0}{(2c_{f0})^{-1/2} + (2\kappa)^{-1}} \frac{\Delta h}{\ell_g}. \tag{3.3}$$

In practice, m_ℓ is often estimated directly from the experimental results for the smallest riblets, because of the uncertainty about the real geometry details like tip-rounding, which greatly affects the viscous performance. Analogous slopes can be defined for s^+ and h^+, and the influence of the viscous regime on the drag-reduction curve should, in principle, be limited to their values. In particular, since our interest is mostly on the riblet size at breakdown, we will always use drag curves normalized with the viscous slopes, computed either directly from Stokes calculations or from the experiments. Note that this normalization does not modify the location of the optimum drag reduction, but that it simplifies its identification by removing the influence of all the other scaling parameters. This is done in figures 4(*a*)–4(*c*) for a variety of riblet geometries and for three different size measures, and it is clear that ℓ_g^+ provides the best collapse for the breakdown dimensions at small sizes. As a practical aside, figure 4(*c*), together with a computational Stokes' estimate of the viscous m_ℓ, can be used as a tool for engineering predictions of drag reduction in a wide range of ℓ_g^+. For the

geometries included in the figure,

$$DR_{max} \approx 0.83\, m_\ell\, \ell^+_{g,opt}, \tag{3.4}$$

where the optimum riblet spacing can be approximated by its mean value $\ell^+_{g,opt} = 10.7$, as in figure 4(*d*). This is particularly useful for conditions such as the aforementioned tip rounding, which has a strong influence on the viscous slope but modifies the groove cross-section relatively little (Walsh 1990*a*; García-Mayoral & Jiménez 2011).

In spite of the good collapse of figure 4(*c*), it should be stressed that ℓ^+_g may not be an adequate parameter to characterize the performance of unconventional geometries, such as the fibres and seal fur mentioned above, for which A_g is difficult to define, or the T-shaped riblets cited by Walsh (1990*b*). Taking the latter as an example, it is clear that, as the wall-parallel segments of the T-fences widen and the space between their tips is reduced, the grooves become increasingly isolated from the overlying flow, while still maintaining the same ℓ^+_g. In the limit of fully sealed grooves, the geometry would behave as a flat surface, and modifying ℓ^+_g would have no performance impact. The present rule can only be considered an empirical approximation valid for geometries that are not too different from the experimental 'conventional' riblets, such as the triangular, trapezoidal, blade, and scalloped riblets frequently proposed in the literature, in which a groove fully exposed to the outer flow can clearly be defined.

It is therefore important to understand the nature of the viscous breakdown, to clarify the reason for the present collapse, and to find whether it can be extended to other geometries, either using ℓ^+_g or other related parameter. For that purpose, we have conducted the numerical experiments described next.

4. The numerical method

In this section we outline the method used to solve the incompressible Navier–Stokes equations in a parallelepiped that includes the walls of a ribbed channel, periodic in the two wall-parallel directions and of half-width δ, at a Reynolds number $\delta^+ \approx 180$. The wall geometry chosen for our experiments consists of rectangular riblets with depth-to-spacing ratio $h/s = 0.5$, blade thickness $t/s = 0.25$ and $\ell_g/s \approx 0.61$, for which Stokes calculations give a protrusion height $\Delta h/\ell_g = 0.095$, and an offset for the streamwise velocity $\Delta_u/\ell_g = -0.16$. From a drag-reduction perspective, this geometry is far from optimal, with a maximum expected reduction of about 6 %, but it requires a lower numerical resolution than sharper configurations, reducing the computational costs and improving the accuracy of the results. Previous DNSs of riblets (Choi *et al.* 1993; Chu & Karniadakis 1993; Stalio & Nobile 2003; Orlandi, Leonardi & Antonia 2006; El-Samni, Chun & Yoon 2007) were usually conducted in channels with riblets in only one wall, with the opposite wall used as the reference to measure friction. However, although that arrangement may be useful in comparing channel simulations among themselves, it is inconvenient when trying to relate computations to experiments on boundary layers. If only one wall is ribbed, the flow is asymmetric, and the friction velocities are different for both walls. This leads to different friction Reynolds numbers and wall units at either side of the channel, which, if not taken into account, would lead to errors in the calculation of the riblet sizes s^+ or ℓ^+_g. It is also unclear which value should be used for the free-stream velocity in the friction coefficient, to make it comparable with boundary layers. These effects are negligible for moderate or high Reynolds numbers, but they can be substantial at the relatively low Reynolds numbers of most DNSs, especially when dealing with the relatively weak effects of most riblets. To avoid those potential errors, our simulations include

riblets in both walls and use as reference a smooth-wall channel with the same mass flux between the two planes defined by the riblet tips. We also take as reference velocity the one at the centreline.

When the spacing between riblets is in the drag-reducing range, the accurate representation of the flow near the ribbed walls requires a finer grid than the one required for the body of the channel. To alleviate the computational cost, our grid is divided into three blocks, one near each wall in which the resolution is fine enough to represent the riblets, and a coarser central one in which the resolution is only enough to simulate the turbulence. The walls are modelled with the immersed-boundary technique detailed below.

The velocities and pressure are collocated and expanded in Fourier series along the two wall-parallel directions x and z. The differential operators are approximated spectrally along those directions, and the nonlinear terms are de-aliased using the 2/3 rule. The spatial differential operators in y are discretized using second-order, centred finite-differences on a non-uniform grid. The grid spacing in y is coarsest at the centre of the channel, $\Delta y^+_{max} \approx 3$, and finest near the walls, $\Delta y^+_{min} \approx 0.3$, remaining nearly constant within the riblet grooves. The number of x modes is set so that $\Delta x^+ \approx 6$ in the three blocks, expressed in terms of collocation points. In the central block of the grid, the resolution along z is just enough to capture the smallest turbulent scales, $\Delta z^+ \approx 2$, while the number of z modes in the blocks containing the riblets is always set to 24 physical collocation points per riblet. This resolution is similar to those of Goldstein, Handler & Sirovich (1995) and Goldstein & Tuan (1998), who also used a combination of spectral methods and immersed boundaries for their riblet DNSs. In our simulations, the riblet surfaces are chosen to coincide with collocation points. Depending on the case, the spanwise grid is between 1.5 and 6 times finer in the wall blocks than in the central one. The additional Fourier modes of the wall blocks require boundary conditions at the interface with the central block, where they disappear. We impose at those points that the three velocities and $\partial p/\partial y$ vanish, and require that the wall blocks extend far enough into the channel for those four quantities to have decayed to negligible levels at the interface. This condition is checked *a posteriori* and found to be satisfied beyond one or two riblet heights above the plane of the riblet tips.

Incompressibility is enforced weakly (Nördstrom, Mattsson & Swanson 2007). If we denote the velocity divergence by $D = \boldsymbol{\nabla}\cdot\boldsymbol{u}$, the equations of motion are

$$\frac{\partial \boldsymbol{u}}{\partial t} + \boldsymbol{u}\cdot\boldsymbol{\nabla}\boldsymbol{u} = -\boldsymbol{\nabla} p + \frac{1}{Re}\nabla^2\boldsymbol{u}, \tag{4.1}$$

$$\frac{\partial D}{\partial t} = -\lambda_D D + \frac{1}{Re_D}\nabla^2 D, \tag{4.2}$$

where λ_D and Re_D are positive coefficients, so that D is driven continuously and exponentially towards zero, instead of being required to vanish strictly. This weak form of the incompressibility condition allows us to use a collocated grid, while eliminating the usual 'chequerboard' problem (Ferziger & Perić 1996).

The temporal integrator is a fractional-step, pressure-correction, three-substep Runge–Kutta, which only corrects the pressure in the final step (Le & Moin 1991):

$$\left[1 - \Delta t\frac{\beta_k}{Re}L\right]\boldsymbol{u}^n_k = \boldsymbol{u}^n_{k-1} + \Delta t\left[\frac{\alpha_k}{Re}L\left(\boldsymbol{u}^n_{k-1}\right) - \gamma_k N\left(\boldsymbol{u}^n_{k-1}\right) - \zeta_k N\left(\boldsymbol{u}^n_{k-2}\right) - (\alpha_k+\beta_k)G(p^n)\right], \quad k = 1, 2, 3 \tag{4.3}$$

$$\hat{D}^{n+1} = D\left(\boldsymbol{u}_3^n\right), \tag{4.4}$$

$$D^{n+1} = D^n + \Delta t\, F\left(D^n + \frac{\Delta t}{2} F\left(D^n\right)\right), \tag{4.5}$$

$$L(\phi^{n+1}) = -\frac{1}{\Delta t}\left(D^{n+1} - \hat{D}^{n+1}\right), \tag{4.6}$$

$$p^{n+1} = p^n + \phi^{n+1}, \tag{4.7}$$

$$\boldsymbol{u}^{n+1} = \boldsymbol{u}_3^n - \Delta t G \phi^{n+1}, \tag{4.8}$$

where k is the Runge–Kutta substep, $\boldsymbol{u}_0^n = \boldsymbol{u}^n$, N is the de-aliased convective term operator, D, G and L are the discretized divergence, gradient and Laplacian operators, and $F(D) = -\lambda_D D + L(D)/Re_D$. The coefficients α_k, β_k, γ_k and ζ_k are those in Le & Moin (1991).

To model the no-slip condition at the riblet walls, we use the direct-forcing immersed-boundary technique of Iaccarino & Verzicco (2003). Numerically, the immersed-boundary condition

$$\frac{\boldsymbol{u}^{n+1} - \boldsymbol{u}^n}{\Delta t} = \frac{\boldsymbol{V} - \boldsymbol{u}^n}{\Delta t}, \tag{4.9}$$

where $\boldsymbol{V}$ is the desired velocity at the forcing points, is approximated by

$$\left[1 - \Delta t \frac{\beta_k}{Re} L\right] \boldsymbol{u}_k^n = \left(\boldsymbol{V}_{k-1}^n - \boldsymbol{u}_{k-1}^n\right) + \left[1 - \Delta t \frac{\beta_k}{Re} L\right] \boldsymbol{u}_{k-1}^n, \tag{4.10}$$

which, in practice, is a modification of (4.3) at the forcing points. In principle, the term $\boldsymbol{V}_{k-1}^n$ could be explicitly calculated from $\boldsymbol{u}_{k-1}^n$ by linear interpolation (García-Mayoral & Jiménez 2007), but in our rectangular riblets, whose surface is formed by grid points, it is always zero. In addition, (4.10) is used to force the velocities to vanish at all the points within the solid part of the riblets, and there is a notional flat boundary at the level of the groove floors, where the velocities and $\partial p/\partial y$ are also required to vanish. The resulting velocities at the riblet surface are not exactly zero, but they are at worst of order $0.1u_\tau$ for u, and $0.01u_\tau$ for v and w, which is in both cases roughly one order of magnitude smaller than the corresponding values in the first grid point away from the surface. They are mostly due to the imposition of the immersed-boundary method before the pressure correction step, a feature common to other fractional-step implementations (Fadlun *et al.* 2000).

The variable time step is adjusted to maintain fixed convective and viscous Courant–Friedrichs–Lewy numbers, $\mathrm{CFL}_C = 0.5$ and $\mathrm{CFL}_V = 2.5$ respectively, so that

$$\Delta t = \min\left\{ \mathrm{CFL}_C \left[\frac{\Delta x}{\pi|u|}, \frac{\Delta z}{\pi|w|}, \frac{\Delta y}{|v|}\right], \quad Re\,\mathrm{CFL}_V \left[\frac{\Delta x^2}{\pi^2}, \frac{\Delta z_c^2}{\pi^2}, \frac{\Delta z_r^2}{\pi^2}, \frac{\Delta y_{min}^2}{4}\right] \right\}, \tag{4.11}$$

where the subscripts 'c' and 'r' refer to the central and riblet blocks. The parameters λ_D and Re_D are chosen at each time step so that (4.5) is stable for Δt given by (4.11). The resulting divergence in the flow is never higher than $D^+ \approx 2 \times 10^{-4}$, which should be compared with the magnitude of other velocity gradients. For example, the magnitude of the vorticity is $|\omega^+| \approx 0.05$–0.2.

The channel half-height is $\delta = 1$ in all cases, including in the smooth reference one, and is defined as the distance from the centre of the channel to the riblet tips, while the domain half-height is slightly larger, extending to the groove floors. The viscosity is always $\nu = 1/3250$, chosen so that $\delta^+ \approx 180$ in the smooth case. The time-dependent

mean streamwise pressure gradient P_x is adjusted to ensure a constant flow rate Q in $y \in (0, 2\delta)$. This is done at each substep by a correction ΔU_k^n to the instantaneous plane-averaged streamwise-velocity profile U_k^n,

$$\left[1 - \Delta t \frac{\beta_k}{Re} \frac{\partial^2}{\partial y^2}\right] \hat{U}_k^n = -\Delta t\,(\alpha_k + \beta_k), \tag{4.12}$$

$$\Delta P_x = \frac{Q - Q_k^n}{\hat{Q}_k^n}, \tag{4.13}$$

$$\Delta U_k^n = \Delta P_x \hat{U}_k^n, \tag{4.14}$$

where $\hat{Q}_k^n$ is the flow rate associated with the auxiliary $\hat{U}_k^n$, and Q_k^n is the flow rate of the uncorrected U_k^n. For simplicity, $\hat{U}_k^n$ is only defined for $y \in (0, 2\delta)$, and its boundary conditions are $\hat{U}_k^n = 0$ at the riblet tip planes, so there is no correction within the grooves owing to the constant Q constrain. This entails a very small error because the corrections on P_x and U_k^n are several orders of magnitude smaller than their uncorrected values. Except for that small error, the procedure is equivalent to imposing on the discretized Navier–Stokes problem (4.3)–(4.8) the time-dependent pressure gradient required to obtain a constant flow rate, which is the procedure used in most channel DNSs, both smooth and rough.

Besides the turbulent smooth channel computed as a reference, in which the walls were also implemented using immersed boundaries, the code was validated on a two-dimensional Taylor–Green vortex and on the transition of the wake of a laminar cylinder. The Taylor–Green vortex was used to test the time accuracy of the integrator, which was found to be second order for the velocity and first order for the pressure, with the second-order velocity errors mostly associated with viscous terms, as in most incompressible fractional-step Runge–Kutta schemes (Simens *et al.* 2009). The cylinder flow is a stringent test for immersed-boundary methods, since the detachment and transition to an unsteady wake are very sensitive to the geometry of the obstacle (Linnick & Fasel 2005). In our tests, the flow transitioned at $Re \approx 42$, defined with the cylinder diameter, which is in good agreement with the experimental range $Re = 40$–49 (Roshko 1953; Williamson 1989). The code was further tested by reproducing one of the simulations with triangular riblets in Choi *et al.* (1993).

The parameters of our main set of simulations are given in table 1. The number of riblets in the box is varied to span the full drag-reducing range. To our knowledge, this is the first time that such a systematic parameter sweep has been undertaken for numerical riblets, except perhaps that by El-Samni *et al.* (2007), who included five different riblet sizes. Notice that L_z is increased slightly in case 17S, to obtain the desired ℓ_g^+ while keeping the fixed geometric resolution of the riblets. In addition, cases 10S and 17S were repeated while independently doubling N_x, N_{z_r}, and the length and width of the channel, to check whether the simulations could be considered converged with respect to the grid and box sizes. The results agreed well with the ones used in the paper. One of those cases, 17D, has been included in table 1 because it will be used in figure 14. The simulations in our main set were run for roughly 150 eddy turn-over times, δ/u_τ, of which the first few were discarded to avoid the effects of the initial transients on the statistics. They had to be run for such long times to reduce the effect of the wall-friction oscillations, which, for our relatively small simulation boxes, are of the order of 10 %.

Case	No. of ribs	ℓ_g^+	s^+	δ^+	L_x	L_z	N_x	N_{z_c}	N_{z_r}
0S	0	0	0	189.31	2π	$2\pi/3$	192	192	192
5S	48	4.95	8.09	185.37	2π	$2\pi/3$	192	192	1152
7S	32	7.38	12.05	184.11	2π	$2\pi/3$	192	192	768
10S	24	9.80	16.01	183.47	2π	$2\pi/3$	192	192	576
13S	18	13.04	21.29	182.99	2π	$2\pi/3$	192	192	432
15S	16	14.74	24.07	183.91	2π	$2\pi/3$	192	192	384
17S	15	17.40	28.41	186.03	2π	$2\pi/2.74$	192	192	360
20S	12	20.46	33.41	191.42	2π	$2\pi/3$	192	192	288
17D	30	17.55	28.67	187.71	2π	$4\pi/2.74$	192	384	720

TABLE 1. DNS parameters. ℓ_g^+ is the square root of the groove cross-section, s^+ is the riblet spacing and δ^+ is the friction Reynolds number, L_x and L_z are the channel length and width, and N_x, N_{z_c} and N_{z_r} are the number of collocation points in the streamwise and spanwise directions, for the central and wall blocks respectively.

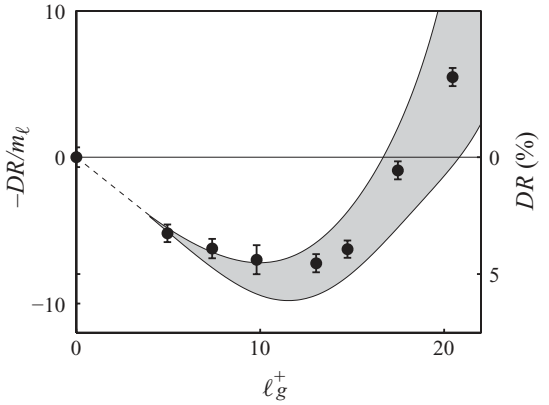

FIGURE 5. Drag-reduction results from DNSs of channels with rectangular riblets. ●, results normalized using (3.3), with protrusion heights obtained from a second-order finite-difference Stokes simulation with the same effective resolution as the DNSs, and the value for μ_0 from Jiménez (1994). The error bars have been estimated from the time history of DR, following Hoyas & Jiménez (2008). The shaded area is the envelope of the experimental data in figure 4(*c*).

5. DNS results and discussion

Figure 5 compares the drag reduction obtained for the numerical cases 0S to 20S with the experimental data discussed in § 3, with reasonably good agreement.

The definition of the friction coefficient deserves some comment. It was noted by Luchini (1995) that the friction coefficient of internal flows is harder to define than that of external boundary layers. In the latter, a reasonable procedure is to normalize the wall friction with the free-stream velocity, which is also the quantity of interest in vehicular applications. In internal flows, the practical quantity is the mass-flow rate, but, if it is used to normalize c_f, there is an ambiguity as to which hydraulic radius should be used to convert the flow rate into a bulk velocity. Luchini (1995) remarked that different 'reasonable' choices could result in changes of the friction coefficient comparable to those expected from the riblets themselves, with the neutral choice being measuring the hydraulic radius from the virtual origin Δ_u.

On the other hand, it follows from the discussion in § 3 that the physically relevant definition of drag change should be based on the offset ΔB of the logarithmic velocity profile, which, if we assume that surface manipulations only modify the near-wall region, is equivalent to the change in the maximum mean velocity U_δ^+. The only corrections are those associated with the denominator of (3.2), which depends weakly on the Reynolds number. That is why in this paper we use the centreline velocity to normalize the friction coefficient, rather than the mass flux. The friction Reynolds number is kept approximately constant by the procedure of fixing the flux among the different cases, and the effect of any small change should only manifests itself in the change of c_{f0} in the denominator of (3.2), which would yield at most a 1 % change in drag.

The friction itself is defined in terms of the mean pressure gradient P_x. In the case of smooth walls, the skin friction can be obtained by extrapolating to the wall the total stress, $\tau(y) = -\langle uv \rangle + \nu \partial_y \langle u \rangle$, which is linear in y with slope P_x. The brackets $\langle\rangle$ stand for averaging over wall-parallel planes and time. Equivalently, it follows from the integrated streamwise momentum equation that

$$2L_z \tau_w = -A_c P_x, \tag{5.1}$$

because the friction in both walls has to compensate the effect of P_x over the cross-sectional area $A_c = 2\delta L_z$. The result

$$\tau_w = -\delta\, P_x \tag{5.2}$$

can be derived either from the extrapolation of $\tau(y)$ or from (5.1).

In cases with riblets, the wall friction is not exerted at a constant y-plane to which $\tau(y)$ can be extrapolated, but we can use (5.1) as long as A_c is the real channel cross-section, including the open section of the grooves. Equivalently, since the total stress is still linear above the riblet tips, τ_w can be computed by extrapolating $\tau(y)$ to the level $y = \delta - \delta'$, where $A_c = 2\delta' L_z$, which is the y-plane at which a smooth wall would have to be located for a channel of area A_c. The resulting τ_w is the total friction exerted per unit streamwise length and channel span, and is thus the correct quantity to compare with the friction on a smooth wall when estimating drag reduction. For our test geometry, $\delta' = \delta + 3h/4$. Note that, if those corrections are not taken into account and τ_w is estimated by extrapolating the total stress to $y = 0$, the relative error in c_f would be of order $(\delta - \delta')/\delta \sim h/\delta$. For typical values of $\Delta c_f / c_f \approx 0.1$, that error would only be negligible if $h/\delta \ll 0.1$, which is not our case.

5.1. *The conditional flow*

To elucidate the structure of the flow near the ribbed surface, we have compiled flow statistics conditioned on the spanwise position across the riblet. Figure 6(a, b) portrays the conditionally averaged crossflow inside and immediately above a riblet groove, for several riblet sizes. The panel for $\ell_g^+ = 0$ is the two-dimensional Stokes crossflow used for the computation of the protrusion height. For non-zero values of ℓ_g^+, the crossflow is averaged over identical spanwise locations with respect to each riblet, as well as over time and x, but, since that procedure only recovers a weak secondary flow, the statistics are also conditioned on the mean direction of the crossflow in the plane immediately above the riblet tips. The flow over individual grooves is characterized as either 'rightward' or 'leftward', and the statistics for the two directions are combined by adding the specular image of the mean leftward flow to the rightward one. Note that this procedure generates statistics that are not

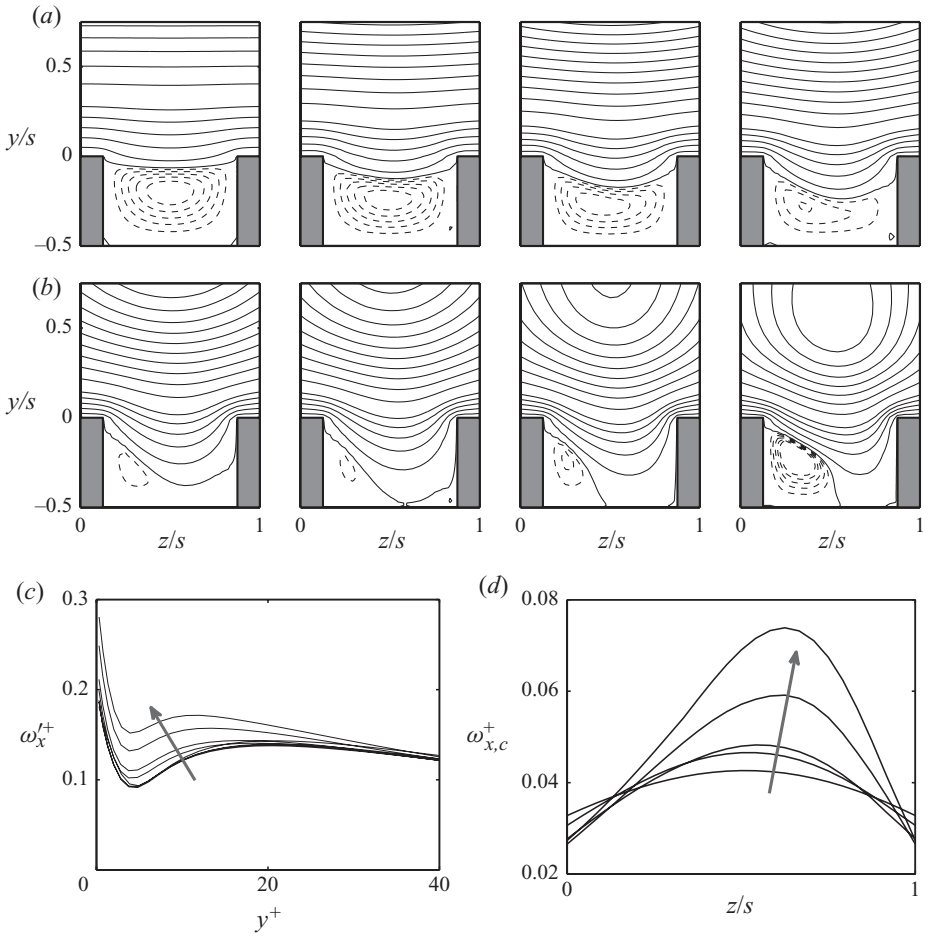

FIGURE 6. (a, b) Streamfunction of the conditionally averaged crossflow above and within the riblet grooves, conditioned to a mean rightward flow in the plane immediately above the riblet tips. From left to right and top to bottom, $\ell_g^+ = 0$ and cases 5S to 20S. The case $\ell_g^+ = 0$ is a two-dimensional Stokes simulation. To facilitate the comparison between different cases, the streamfunction has been scaled with u_τ and with the riblet height h. ——, rightward flow with streamfunction values $0.05 \times [0(0.2)1]^2$ and $0.10(0.05)0.60$. – – – –, clockwise recirculation flow, with streamfunction values $-2 \times [0.2(0.2)1] \times 10^{-3}$. ($c$) Fluctuation of the streamwise vorticity as a function of the distance to the riblet peak plane, for cases 0S to 20S. (d) Maximum conditioned streamwise vorticity, as a function of the z-position across the riblet span, for cases 10S to 20S. The arrows in (c) and (d) indicate increasing ℓ_g^+.

periodic with the riblet spacing, because the flow over each riblet is conditioned to a particular orientation, while those over the neighbouring ones are not.

Figure 6(*a,b*) shows that there is a weak recirculation bubble in the riblet groove, which is especially clear in the Stokes case (first panel in figure 6*a*), but which persists up to the viscous breakdown, becoming increasingly asymmetric for the larger riblets.

At the same time, other changes occur in the outer flow. The increasing curvature of the conditional streamlines suggests that a mean vortex settles above the groove and drifts towards the wall as the riblet size increases. It turns out that the drift is mostly due to the change in the scale of the figures, which are normalized with the riblet height. The vertical position of the vortices is better measured by the unconditioned

root-mean-squared intensity of the vorticity ω_x, which is shown in figure 6(*c*). The quasi-streamwise vortices correspond to the maximum away from the wall and slowly approach the wall as the riblets get larger, but they never get closer than $y^+ \approx 10$–15. The simplest interpretation of the velocity fields in figure 6(*a*,*b*) is that the vortices tend to linger on top of the grooves. This tendency can be measured by the modulation in z of the conditionally averaged maximum streamwise vorticity, $\max_y \langle \omega_x \rangle_c$, where the brackets now refer to the conditional mean. This quantity is shown in figure 6(*d*). It is maximum above the grooves and minimum above the riblet tips. Its modulation is negligible for the smallest riblets and increases with the riblet size, showing that the vortices get increasingly localized above the grooves for the larger riblets.

Goldstein *et al.* (1995) and Goldstein & Tuan (1998) suggested that one of the effects of the riblets was to order the turbulent flow near the wall by preventing the spanwise motion of the streamwise vortices, inhibiting the instability of the streamwise-velocity streaks, and eventually the bursting. They conjectured that this effect would be part of the drag-reduction mechanism. The vortex localization observed in figure 6(*d*) supports the flow-ordering idea, but it is interesting that the localization is weak for the riblets that actually reduce drag and strongest for those that increase it, suggesting that other phenomena may be more important for the drag evolution.

The actual lodging of the vortices inside the grooves, which was documented by Choi *et al.* (1993) and Lee & Lee (2001) for grooves with $\ell_g^+ \gtrsim 25$, and proposed as a mechanism for the drag deterioration, is not observed in the present simulations. Figures 5 and 6(*a*,*b*) suggest that, if it happens at all, it probably only does for very large riblets in the drag-increasing regime, rather than in those in the neighbourhood of the performance optimum. In that sense, it should probably be considered a consequence, rather than the cause, of the penetration of the outer flow into very large grooves.

On the other hand, although it could have been expected that the recirculation bubbles would isolate the valley floor from the overlying flow, keeping the high-momentum fluid away from the groove walls, it is somewhat surprising that all the changes in the crossflow have a relatively small effect on the streamwise velocity, which is the component responsible for the friction. That is seen in figure 7(*d*), which portrays the mean slip velocity U_0 at $y = 0$, as a function of the riblet size, and shows that the linear Stokes approximation holds for the longitudinal flow throughout the whole range of our simulations, at least in the mean. Averaging the Stokes assumption (2.2) over the streamwise direction and time implies that the mean velocity of the boundary layer approaches the wall with an effective slip velocity

$$U_0^+ \equiv U^+(y = 0) = -\Delta_u^+, \tag{5.3}$$

which is represented by the solid line in figure 7(*d*).

The reason is probably that the recirculation bubbles in figure 6(*a*,*b*) are relatively weak. The magnitude of the conditioned spanwise velocity at the horizontal mid-plane of the riblet grooves in figure 6(*a*,*b*), $y = -h/2$, never exceeds $0.04\,u_\tau$, and the mean streamwise velocity within the grooves follows the same universal curve $U(y/h)/U_0$ within a few per cent for all the riblets in our simulations. Similarly, the mean velocity gradient at the bottom of the groove is always $(\partial_y U)^+ \approx 0.15$.

That low shear at the bottom of the grooves is not enough to guarantee drag reduction, as seen in the case $\ell_g^+ = 0$, where the drag reduction is zero because the low shear within the groove is compensated by the higher one at the peaks. In fact, the approximately universal scaling of the streamwise velocity inside the grooves suggests that the reason of the drag reduction is not so much that the friction

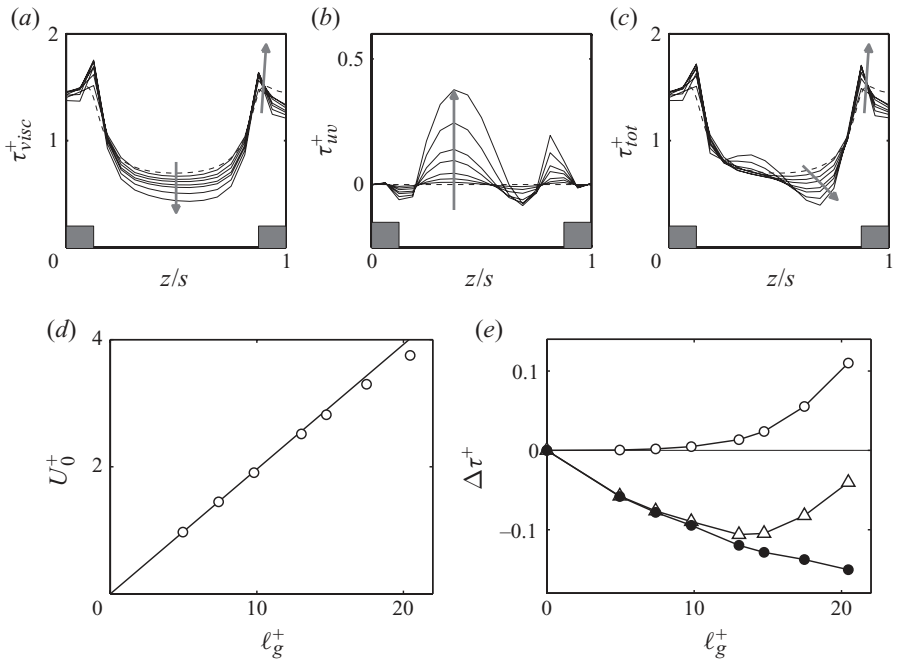

FIGURE 7. Conditionally averaged viscous (*a*), Reynolds (*b*) and total (*c*) shear stresses at the x–z plane just above the riblet tips, as a function of the spanwise position with respect to the riblets. The arrows indicate increasing ℓ_g^+. The dashed line corresponds to the Stokes two-dimensional simulations for $\ell_g^+ = 0$. The rectangles at the bottom of the figures mark the z-location of the riblet tips. Each flow is normalized in its own wall units. (*d*) Mean slip velocity at the riblet-tip plane, compared with the Stokes result (5.3), represented by the solid line. (*e*) Integrated average stresses at the same x–z plane, as a function of ℓ_g^+; –●–, viscous stress; –○–, Reynolds stress; –△–, total stress. The difference between the total stress portrayed here and the results in figure 5 is due to the pressure drop within the grooves, which is not accounted for here, and whose contribution increases with groove size.

decreases, but that the slip augments the velocity of the free stream, thus decreasing the friction coefficient $2\tau_w/U_\delta^2$. Of course, both interpretations are essentially the same, depending on the units used to express the result, and the question will be examined quantitatively in § 5.2.

Before doing that, we can gain some insight on how the riblets affect the distribution of the friction by examining the conditional statistics of the viscous, Reynolds, and total streamwise stresses on the x–z plane just above the riblet tips. Figures 7(*a*)–7(*c*) portray the conditionally averaged stresses normalized with the friction velocity of each ribbed surface. The figures show that the dominant stress on that plane is always the viscous one, $\tau_{visc} = \nu\partial_y\langle u\rangle_c$, which partially compensates its high value over the tips with a lower one above the grooves. We have already mentioned that the net effect vanishes in the case $\ell_g = 0$, and figures 7(*a*)–7(*c*) show that, although the viscous contribution decreases over the groove as the riblet size increases, the effect is partly compensated by the Reynolds stress, $\tau_{uv} = -\langle uv\rangle_c$, which becomes significant for the larger riblets. The ratio between the contributions to the total skin friction of the tips and of the grooves remains relatively unchanged over the range of our simulations, in agreement with the previous observation that the streamwise flow in the groove remains dominated by viscosity. The partial transfer of viscous to Reynolds stress

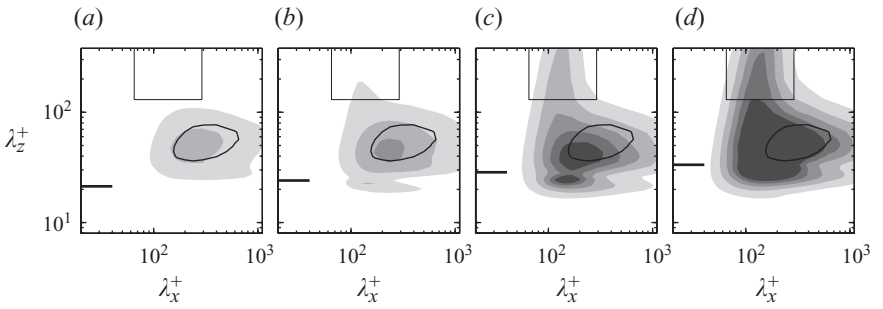

FIGURE 8. Premultiplied two-dimensional spectra of v^2 at $y^+ \approx 5$. From (*a*) to (*d*), cases 13S, 15S, 17S and 20S. The contour increments are $0.003\,u_\tau^2$. The superimposed solid contours correspond to the smooth-wall case and the level $0.003\,u_\tau^2$. The thick horizontal line to the left of the plots marks the riblet spacing. The rectangular area indicates the region of the spectrum considered in figure 12.

reflects the modification of the distribution of streamwise and wall-normal velocities near the plane of the riblet tips, but it does not reach deep into the grooves.

This does not mean that the drag remains constant, since our simulations cover the whole range from drag reduction to drag increase. The net contributions of the two stress components, now expressed in terms of the constant friction velocity of the smooth channel, can most clearly be appreciated in figure 7(*e*). The figure shows that the net viscous stress decreases almost linearly with ℓ_g^+, while the Reynolds stress increases slowly at first and faster for the larger ℓ_g^+. In the cases near the maximum drag reduction, the Reynolds stress compensates the decrease of the viscous one and the drag reduction saturates. For riblets larger than the optimum, the drag reduction begins to degrade because the mean Reynolds stress increases further, and, for case 20S, the contribution of the Reynolds stress is so large that the drag reduction becomes a drag increase. The breakdown is therefore associated with the appearance of inertial effects, but the discussion in the previous paragraph suggests that they are concentrated near or above the plane of the tips, rather than within the grooves. They are discussed in the next section.

5.2. *Spectral analysis*

The main difference between flows in smooth and ribbed channels is the higher fluctuation intensities of the latter immediately above $y = 0$ (not shown, but see figures 9 and 12). In the same way, the transverse Reynolds stress $-\langle uv \rangle$ increases over riblets, especially over the larger ones (see figure 7*b*). Both things are to be expected from the relaxation of the wall boundary conditions above the riblet grooves, and are consistent with the discussion in the previous section. More interesting is the spectral distribution of those higher intensities.

Figures 8–10 contain examples of two-dimensional spectral energy densities over wall-parallel planes for cases 13S to 20S, representing how the energy of the different velocity components is distributed in the λ_x^+–λ_z^+ wavelength plane. Those are the riblets beyond the viscous breakdown, and the ones whose spectra differ most from those of the smooth channel, which are superimposed for comparison as solid lines.

Figure 8 shows the spectral density of v^2 at $y^+ \approx 5$. As the riblet size increases beyond the optimum spacing, energy accumulates in a spectral region near $\lambda_x^+ \approx 150$ that extends over all the spanwise wavelengths longer than $\lambda_z^+ \approx 50$, and which therefore represents very wide structures. The same can be seen in the spectra of the

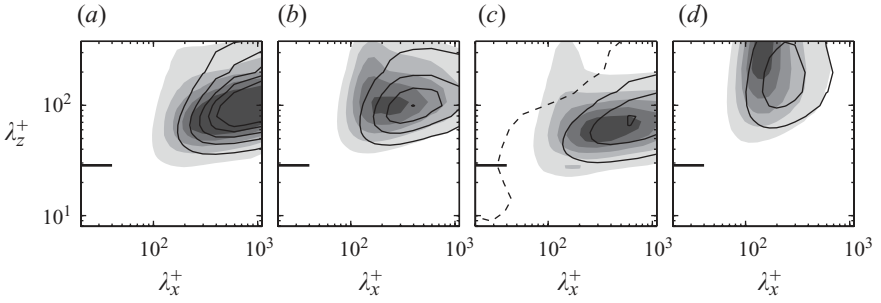

FIGURE 9. From (*a*) to (*d*), premultiplied two-dimensional spectra of u^2, w^2, uv and p^2, at $y^+ \approx 5$, for case 17S. The corresponding v^2 spectrum is plotted in figure 8. The contour increments are, in wall units, 0.09, 0.026, 0.005 and 0.2 respectively. The superimposed solid contour lines correspond to the smooth-wall case, with the dashed contour line corresponding to $uv = 0$. The thick horizontal line to the left of the plots marks the riblet spacing.

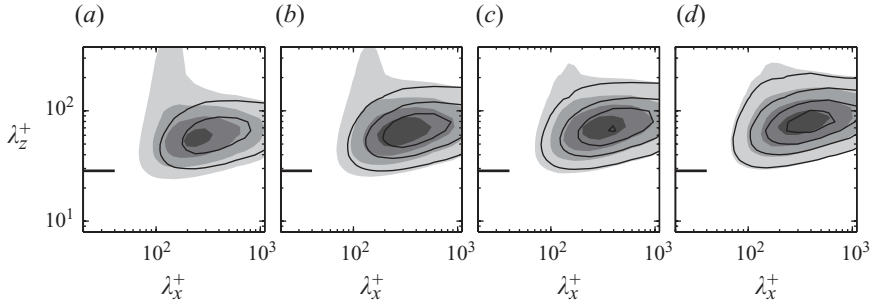

FIGURE 10. Premultiplied two-dimensional spectrum of v^2 for case 17S. From (*a*) to (*d*), at heights $y^+ \approx 10$, 15, 19 and 25. The same spectrum is plotted for $y^+ \approx 5$ in figure 8. The superimposed solid contour lines correspond to the smooth-wall case. The contour increments are 0.010, 0.015, 0.020 and $0.025\,u_\tau^2$ for increasing y^+. The thick horizontal line to the left of the plots marks the riblet spacing.

other flow variables, which are given in figure 9 for case 17S. The new spectral region exists only for heights below $y^+ \approx 15$–20, depending on the variable considered. The widest vertical range corresponds to v^2, whose spectrum for case 17S is portrayed at different heights in figure 10.

We next focus our analysis on those new structures, which we will treat as being approximately confined to a spectral window delimited by $65 < \lambda_x^+ < 290$ and $\lambda_z^+ > 130$. That window is included in figure 8 for reference. Note that the relatively high lower limit for λ_z^+ implies that we will essentially be studying the effect of riblets on the spanwise-averaged flow, as opposed to the conventional approach used in § 5.1 and elsewhere, which stresses streamwise averages.

Figure 11 portrays the streamwise one-dimensional cospectral density of the uv stress, integrated for $\lambda_z^+ > 130$, and shows that the shear stress carried by the new structures concentrates around $\lambda_x^+ \approx 150$ and $y^+ \approx 4$, and that their contribution grows with the riblet size. The Reynolds stress of the smooth channel is weak and positive (counter-gradient) in that spectral region, but becomes negative and stronger for riblets larger than the optimum.

Although not shown here, the spectra of the extra energy of the velocity components for increasing ℓ_g^+ also scale much better in wall units than when normalized with the

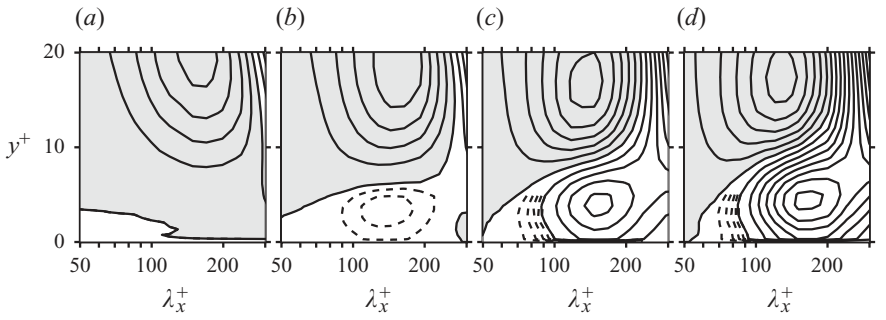

FIGURE 11. Premultiplied streamwise cospectra of the Reynolds stress, $k_x E_{uv}^+$, from (*a*) to (*d*) for cases 0S, 13S, 17S and 20S. The spectra have been integrated in z only for $\lambda_z^+ \geqslant 130$. The solid isolines are spaced by 4×10^{-3}, with the shaded area corresponding to positive values. The dashed isolines correspond to $4 \times [0.2(0.2)0.8] \times 10^{-3}$. Notice that the stresses in the region portrayed are counter-gradient for the smooth-wall case, as can be observed in the uv spectrum in figure 9.

riblet size. The spanwise structures centre around $\lambda_x^+ \approx 150$ and $y^+ \approx 5$ in most cases, although the streamwise velocity is slightly longer, $\lambda_x^+ \approx 200$, and v^2 peaks around $y^+ \approx 10$. Since all our simulations have approximately the same Reynolds number, it is impossible to determine from them whether the spectra collapse in wall or in outer units, although the former seems more plausible given the location of the structures very near the wall, as well as the experimental scaling of the viscous breakdown in wall units. Further support for the wall scaling will be provided in the following section, where we propose a simplified linearized model for the structures.

The energy integrated over the spectral window defined above is given in figure 12 for the three velocity components and for the shear stress. For riblets smaller than 10S, which are not shown in the figure, the results are virtually indistinguishable from the smooth case, but all the fluctuations become stronger beyond the optimum riblet size and keep increasing thereafter.

The additional uv stresses can be directly related to the drag increase beyond the breakdown. Using the subscript 'S' to refer to the reference smooth channel, the momentum balances for the smooth and ribbed channel are, respectively,

$$\tau_{uvS} + \nu \frac{\partial U_S}{\partial y} = u_{\tau S}^2 \frac{\delta - y}{\delta}, \tag{5.4}$$

$$\tau_{uv} + \nu \frac{\partial U}{\partial y} = u_\tau^2 \frac{\delta - y}{\delta'}. \tag{5.5}$$

If we define $u_* = u_\tau (\delta/\delta')^{1/2}$ and integrate these equations over $y \in (0, \delta)$, they can be combined into

$$\int_0^\delta \tau_{uv}^* \, \mathrm{d}y + \frac{\nu}{u_*^2} (U_\delta - U_0) = \int_0^\delta \tau_{uvS}^+ \, \mathrm{d}y + \frac{\nu}{u_{\tau S}^2} U_{\delta S}, \tag{5.6}$$

where $\tau_{uv}^* = \tau_{uv}/{u_*}^2$. Further manipulation results in

$$\frac{\Delta c_f}{c_{f0}} \approx -\frac{\Delta U_\delta^{+2}}{U_\delta^{+2}} = T_1 + T_2 + T_3, \tag{5.7}$$

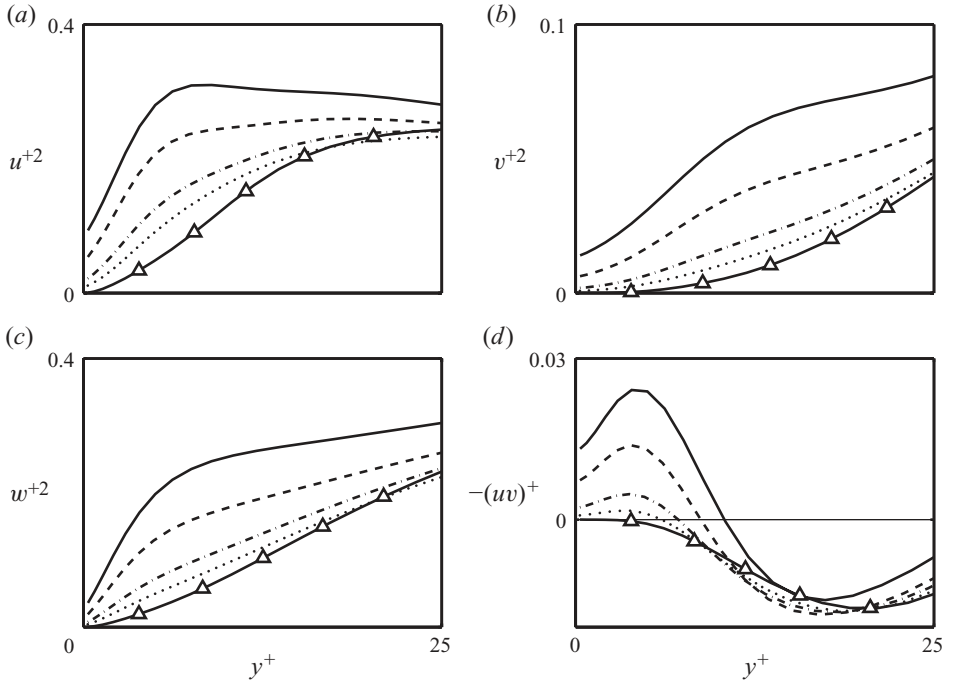

FIGURE 12. Energy contained in the long spanwise structures above riblets. The figures portray the integrals of the spectra of (*a*) u^2, (*b*) v^2, (*c*) w^2 and (*d*) $-uv$, in the region $65 \leqslant \lambda_x^+ \leqslant 290$, $\lambda_z^+ \geqslant 130$. –△–, smooth wall; ·····, 13S; – · – , 15S; – – – –, 17S; ——, 20S.

where

$$T_1 = \left[1 - \frac{\delta U_\delta}{\delta' U_{\delta S}}\right] \left(\frac{U_{\delta S}^+}{U_\delta^+}\right)^2, \tag{5.8}$$

$$T_2 = -\frac{U_0^+}{U_\delta^+}, \tag{5.9}$$

$$T_3 = \frac{\delta\delta^+}{\delta' U_\delta^+} \int_0^1 \left(\tau_{uv}^* - \tau_{uvS}^+\right) \mathrm{d}(y/\delta). \tag{5.10}$$

These three terms are shown in figure 13. The first one is a geometric factor that accounts for the differences in the definition of the two channels, both in height and in mass flux. It should remain small for the decomposition (5.7) to be useful, since otherwise the influence of the Reynolds number mentioned in § 3 should be taken into account. Figure 13 shows that T_1 is always less than a few per cent in our simulations.

The term T_2 represents the slip velocity at the riblet tips, which we have already discussed in § 5.1. It is directly related to the drag-reduction mechanism of the protrusion height and remains proportional to the riblet size over our simulation range. It always reduces skin friction.

The term T_3 represents the effect of the extra Reynolds stresses in the flow above the riblet tips and, owing to the scaling with u_*, its integrand differs from zero only near the wall. Figure 13 confirms that T_3 is the term responsible for the drag degradation. The figure also includes the part of the extra Reynolds stress that is contained in the spectral region that we have associated with the new spanwise structures. It shows

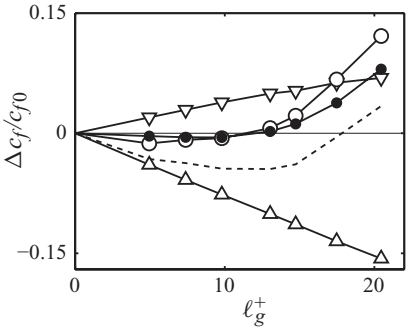

FIGURE 13. Contributions T_1, T_2 and T_3 to the drag-reduction curve, as defined by (5.8)–(5.10). –▽–, T_1; –△–, T_2; –○–, T_3 calculated from the full uv stress. –●–, T_3 calculated considering uv only within $65 \leqslant \lambda_x^+ \leqslant 290$, $\lambda_z^+ \geqslant 50$ and $y^+ \lesssim 35$. – – – –, total drag reduction $T_1 + T_2 + T_3$.

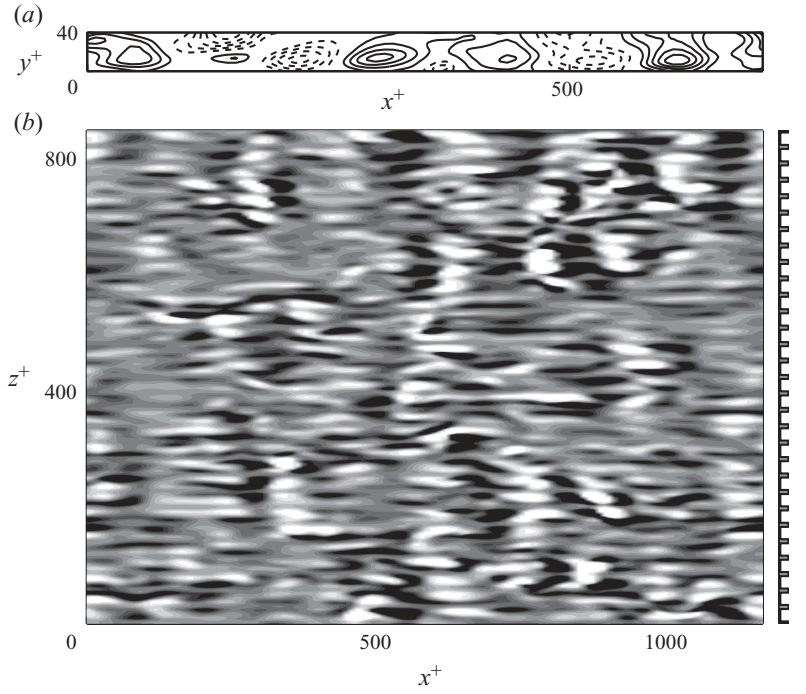

FIGURE 14. (*a*) Instantaneous streamlines of the spanwise-averaged perturbation u–v flow, for case 17D. The solid lines correspond to clockwise-rotating rollers. (*b*) For the same instant, wall-normal velocity at $y^+ \approx 3$. The clear regions represent negative velocities, or flow towards the wall, and the dark regions positive ones. The position of riblet tips and grooves is sketched to the right of the figure.

that this region contains most of the extra stress, strongly suggesting that the new structures are the root cause of the degradation of the drag.

Note that all those structures extend over several inter-riblet spacings. In fact, because they are much wider than their streamwise wavelengths, they can be characterized as spanwise rollers, which are shown in figure 14 for an instantaneous realization of case 17D. Figure 14(*a*) portrays streamlines of the flow averaged over the full span of the simulation box, which is in this case $L_z^+ \approx 850$. The averaged rollers

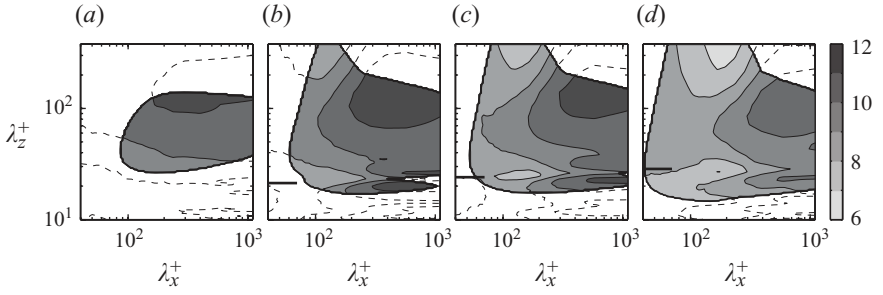

FIGURE 15. (*a*) to (*d*) Convection velocity U_C^+ of v-structures at $y^+ \approx 5$ for cases 0S, 13S, 15S and 17S. Values are significant only within the shaded region and are portrayed elsewhere by dashed contours. The encircling solid line represents the threshold $k_x k_z E_{vv} = 0.001\, u_\tau^2$. Outside of it the v-structures carry very little energy, and the low values of v^2 lead to large uncertainty errors in the calculation of U_C. The thick horizontal line to the left of the plots marks the riblet spacing.

are centred at $y^+ \approx 10$–15, and extend to the wall, even penetrating the riblet grooves. Their streamwise extent is about 50–70 wall units, and the separation between rollers of the same sign is $\lambda_x^+ \approx 150$, consistent with the spectral analysis. That implies aspect ratios for the spanwise-averaged structures in figure 14(*a*) of the order of 10–20, and characterizes them as quasi-two-dimensional in the x–y plane. The structures themselves can be seen in the wall-parallel section in figure 14(*b*), which confirms their spanwise coherence across several riblet grooves. That coherence manifests itself in spite of the presence of the riblet blades, which disrupts the structures with riblet-spacing periodicity. It must however be stressed that figure 14 is merely an instantaneous realization of the flow, and is only included here to help the reader visualize the roller structures. The evidence for those rollers is not this figure, but the discussion on spectra at the beginning of this section, and the corresponding figures 8–12.

To our knowledge, those structures had not been reported before over riblets, but they can probably be found, in retrospect, in some of the visualizations published by previous authors. See, for example, the visualization of v at $y^+ = 8$ above the tips of triangular riblets in figure 20(*b*) of Goldstein *et al.* (1995), or the spanwise lines of velocity reversal within the grooves of similar riblets in figure 30 of Chu & Karniadakis (1993). Even if their conditions are very different from ours, it is interesting that the streamwise wavelengths of the observed structures are in both cases in the range $\lambda_x^+ = 100$–200. It should be noted, however, that we do not observe flow reversal within our grooves.

Although the formation of these structures, perpendicular rather than parallel to the riblets, may seem surprising, it is not completely unexpected. Similar spanwise rollers have been reported over vegetable canopies (Raupach, Finnigan & Brunet 1996; Finnigan 2000), and over permeable (Jiménez *et al.* 2001) and porous walls (Breugem, Boersma & Uittenbogaard 2006). They are typically attributed to Kelvin–Helmholtz-like instabilities due to the relaxation of the impermeability condition at the wall, although quantitative analyses supporting that claim are scarce (Jiménez *et al.* 2001; Py, de Langre & Moulia 2006).

The hypothesis of an instability is reinforced by the advection velocities in figure 15, which were computed as functions of y and of the two wall-parallel wavelengths using the scheme in del Álamo & Jiménez (2009). The advection velocities are noticeably

lower for the spanwise structures than for the spectral region of the regular flow. Near the wall, for $y^+ \lesssim 15$, the latter are of order $10\,u_\tau$, while the former are 6–8 u_τ. The effect becomes more noticeable for the larger riblets and suggests that the structures are not advected by the local flow but correspond to unstable eigenstructures with an extended y-support. The linearized stability of this part of the flow is analysed in the next section.

6. A linear stability model

In this section we propose a model for the aforementioned Kelvin–Helmholtz-like instability, which captures the essential physics involved, including its relation with the riblet geometry.

Since the spanwise rollers are quasi-two-dimensional in x–y, we restrict ourselves to two-dimensional solutions of the linearized Navier–Stokes equations. Denoting by prime superscripts the derivatives with respect to y of the base flow U, we have

$$\frac{\partial u}{\partial t} + U\frac{\partial u}{\partial x} + v\,U' = -\frac{\partial p}{\partial x}, \tag{6.1}$$

$$\frac{\partial v}{\partial t} + U\frac{\partial v}{\partial x} = -\frac{\partial p}{\partial y}, \tag{6.2}$$

where the lowercase symbols are perturbations. The viscous terms are omitted for simplicity, since we are looking for essentially inviscid Kelvin–Helmholtz-like instabilities, on which viscosity would only have a damping effect. Imposing incompressibility, the Rayleigh equation for v is

$$\left(\frac{\partial}{\partial t} + U\frac{\partial}{\partial x}\right)\nabla^2 v = U''\frac{\partial v}{\partial x}, \tag{6.3}$$

for which we seek solutions of the form $v = \widehat{v}(y)\exp[\mathrm{i}\alpha(x - ct)]$.

The problem is solved in a notional domain between the two planes at the riblet tips, $y \in (0, 2\delta)$, and the two dimensionality is preserved by using z-independent boundary conditions that account for the presence of riblets in a spanwise-averaged sense.

Consider the lower wall. The first step is to describe the flow along the grooves, where variables will be denoted by the subscript 'g'. This part of the problem takes place in the real groove geometry in $y \in (-h, 0)$. Since we are interested in the onset of the instability, we will assume that the effective Reynolds number is low and that the longitudinal flow along the grooves satisfies approximately the viscous Stokes equations. Note that this approximation is consistent with the behaviour of the conditioned average streamwise velocity in the direct simulations. We also assume that the longitudinal velocity gradients within the grooves are small with respect to the transverse ones and that the dynamical effect of the transverse velocities can be neglected. In particular, we neglect the variation across the groove of the streamwise pressure gradient and the streamwise contributions of the viscous term. The streamwise momentum equation within the groove is then

$$\frac{\partial^2 u_g}{\partial y^2} + \frac{\partial^2 u_g}{\partial z^2} \equiv \nabla^2_{yz} u_g = \frac{1}{\nu}\frac{\mathrm{d}p_g}{\mathrm{d}x}. \tag{6.4}$$

The velocity satisfies $u_g = 0$ at the groove walls, and we will assume that $\partial u_g/\partial y = 0$ at the plane of the riblet tips. Note that the last boundary condition refers to the perturbations and is not equivalent to assuming that the mean velocity gradient

vanishes at $y = 0$. The assumption is that the streamwise pressure gradient is predominantly balanced by the viscous stresses at the groove walls, rather than by those at the interface with the outer flow. That assumption is especially adequate for small riblets but has to be justified *a posteriori*. For example, consider the solutions in figure 19, which are obtained by coupling the outer flow perturbations to grooves with the no-slip condition at their top interface.The length scales of the perturbations at $y = 0$ scale in wall units, essentially because the true outer boundary condition for the flow within the grooves, $\partial u_g/\partial y = 0$, should have been applied at $y \to \infty$ and involves the overlying velocity profile. In the particular case of the figure, $(\partial u/\partial y)^+ \approx 0.10 u^+|_{y=0}$. On the other hand, the gradients over the walls of the grooves, not shown in the figure, are inversely proportional to the groove diameter. For a typical groove, $(\partial u_g/\partial n)^+ \approx 4u^+|_{y=0}/\ell_g^+$. The assumption that the shear at the groove top can be neglected with respect to that at the walls is valid as long as $\ell_g^+ \ll 40$, which is enough to explore the onset of the instability. The same assumption also allows us to use an inviscid approximation for the outside flow, even while using a Stokes model for the flow in the groove.

The coupling of the grooves and the body of the channel is made by assuming that the outside pressure drives the flow along the grooves and that the transpiration velocity at $y = 0$ is due to the longitudinal variations of the volumetric flux of u_g.

Since the right-hand side of (6.4) is only a function of x and t, we can write

$$u_g = -\left(\frac{1}{\nu}\frac{\mathrm{d}p_g}{\mathrm{d}x}\right) f(y,z), \tag{6.5}$$

where $f(y,z)$ verifies

$$\nabla_{yz}^2 f = -1, \tag{6.6}$$

with boundary conditions identical to those for u_g, so that f depends only on the groove geometry. The streamwise variation of u_g is related to the z-averaged transpiration velocity v at $y = 0$ by integrating the continuity equation over the groove cross-section:

$$\frac{\partial}{\partial x}\int\int_{A_g} u_g \,\mathrm{d}y\,\mathrm{d}z + \int_s v_g|_{y=0}\,\mathrm{d}z = 0, \tag{6.7}$$

$$v|_{y=0} = -s^{-1}\frac{\partial}{\partial x}\int\int_{A_g} u_g \,\mathrm{d}y\,\mathrm{d}z. \tag{6.8}$$

Note that s in (6.8) is the distance between neighbouring riblets, not the width of the groove, because v needs to be averaged over the whole $y = 0$ plane to be used as a boundary condition for (6.3). Introducing (6.5) into (6.8), and assuming that $p|_{y=0} = p_g$, we obtain

$$\left.\frac{\partial^2 p}{\partial x^2}\right|_{y=0} = \frac{\nu}{L_w^3}\, v|_{y=0}\,, \tag{6.9}$$

where

$$L_w^3 = s^{-1}\int\int_{A_g} f \,\mathrm{d}y\,\mathrm{d}z. \tag{6.10}$$

Using (6.9) to eliminate the pressure from the longitudinal momentum equation (6.1) yields the boundary condition

$$\left(\frac{\partial}{\partial t} + U\frac{\partial}{\partial x}\right)\frac{\partial v}{\partial y} = U'\frac{\partial v}{\partial x} \mp \frac{\nu}{L_w^3} v, \tag{6.11}$$

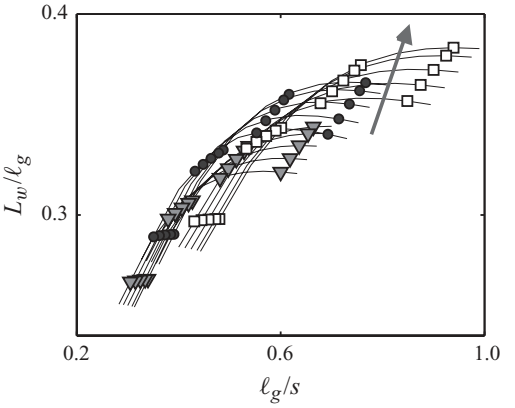

FIGURE 16. Value of the parameter L_w in (6.10), compared with ℓ_g, for: ▼, triangular; ●, scalloped; □, blade riblets. The solid lines connect riblets of the same type with equal tip width and variable depth-to-width ratio, ranging from $h/s = 0.2$ to 1.0, while the arrow indicates decreasing tip width, from $t/s = 0.5$ to 0.02.

where the two signs of the last term apply respectively to the upper and lower walls. If we denote the values of the mean profile at $y = 0$ by U_0 and U_0', (6.11) can be rewritten as

$$(U_0 - c)\frac{\partial \widehat{v}}{\partial y} = \left(U_0' \pm \mathrm{i}\frac{\nu}{\alpha L_w^3}\right)\widehat{v}, \tag{6.12}$$

which shows that U_0 changes only the real part of the advection velocity by a fixed amount. From the point of view of the stability characteristics of the flow, it can be assumed to be zero. The solutions of the system (6.3)–(6.12) depend only on the base flow profile $U(y)$ and on the characteristic penetration length L_w, which is linked to the groove cross-section through the integral in (6.10). The viscosity can be eliminated by expressing everything in wall units. It turns out that, for conventional geometries, L_w is closely linked to our empirical parameter $\ell_g = \sqrt{A_g}$. For example, figure 16 compiles values of L_w computed for triangular, rectangular and scalloped riblets, with depth-to-width ratios between 0.2 and 1.0, and tip widths between 2 % and 50 % of their spacing. It shows that, at least within that range of geometries, ℓ_g and L_w are essentially proportional to each other. The approximation

$$\ell_g \approx 2.8\, L_w \tag{6.13}$$

has less than 10 % error for conventional sharp riblets with $h/s \geqslant 0.4$, providing some theoretical justification for the empirical scaling of the breakdown size discussed in § 3.

6.1. *The piecewise-linear profile*

Before turning our attention to the quantitative analysis of the instability induced by the riblets on a turbulent velocity profile, it is useful to apply the previous formulation to a piecewise-linear base flow

$$\left.\begin{aligned} U(y) &= U_\infty\, y/H, \quad && y < H, \\ &= U_\infty, && y \geqslant H, \end{aligned}\right\} \tag{6.14}$$

where the basic mechanisms are more easily understood. The solutions of (6.3) can then be expressed as combinations of exponentials, $\exp(\pm\alpha y)$, which are continuous

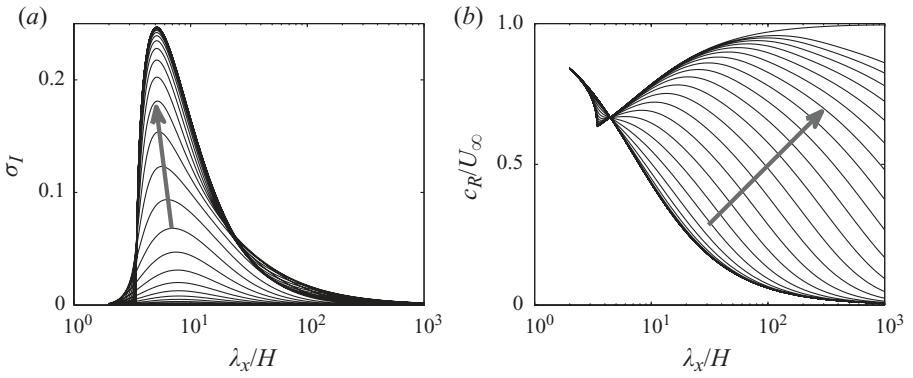

FIGURE 17. (*a*) Growth rate $\sigma_I = \mathrm{Im}(\sigma)$ of the unstable modes given by (6.15), as a function of $\lambda_x/H = 2\pi/\widetilde{\alpha}$. (*b*) Corresponding phase velocities, $c_R/U_\infty = \mathrm{Re}(\sigma)/\widetilde{\alpha}$. Curves are shown for values of $\Lambda = (L_w^3/\nu)(U_\infty\widetilde{\alpha}/H^2) = 10^{[-2(.2)3]}$ and 10^6, with the arrows indicating increasing Λ.

everywhere, vanish at infinity and satisfy a jump condition for their derivatives at the singularity of U'' at $y = H$. The wall boundary condition (6.11) becomes a second-order equation for the temporal eigenvalue,

$$-2\Lambda\sigma^2 + \left[-2\mathrm{i} + \Lambda(1 + 2\widetilde{\alpha} - \mathrm{e}^{-2\widetilde{\alpha}})\right]\sigma + (\Lambda - \mathrm{i})(1 - 2\widetilde{\alpha} - \mathrm{e}^{-2\widetilde{\alpha}}) = 0, \qquad (6.15)$$

where $\widetilde{\alpha} = \alpha H$, $\sigma = (c/U_\infty)\widetilde{\alpha}$ and $\Lambda = (L_w/H)^3(U_\infty H/\nu)\widetilde{\alpha}$. Instability requires that the imaginary part, σ_I, of the eigenvalue be positive.

The smooth wall is recovered for $\Lambda = 0$ and has no unstable modes. For $0 < \Lambda \ll 1$, all the wavenumbers are weakly unstable, with a maximum growth rate, $\sigma_I \approx 0.081\Lambda$, at $\widetilde{\alpha} = 0.80$. In the opposite limit, $\Lambda \gg 1$, the eigenvalues become independent of Λ, and the unstable modes are restricted to the band $0 < \widetilde{\alpha} \lesssim 1.83$. The maximum growth rate is $\sigma_I \approx 0.25$ at $\widetilde{\alpha} \approx 1.23$. The growth rates and phase velocities of the unstable modes for intermediate values of Λ are given in figure 17.

The limit $L_w \gg H$ provides a physical interpretation of the nature of the instability. In this limit, which is essentially $\nu/L_w^3\alpha \ll U_0'$, the boundary condition (6.9) loses the term coming from the wall, and the mean velocity profile can be extended antisymmetrically to $y < 0$, to become a piecewise-linear free shear layer. The problem then has symmetric and antisymmetric eigenfunctions with respect to $y = 0$, of which the symmetric one, $\widehat{v} = \cosh(\alpha y)$, is the well-known unstable Kelvin–Helmholtz sinuous deformation of the free shear layer (Drazin & Reid 1981). The intermediate values of L_w connect these Kelvin–Helmholtz solutions with the stable ones of the impermeable case.

6.2. *The turbulent channel profile*

Although the analysis of the piecewise-linear profile provides qualitative information on the nature of the instability, quantitative comparison with the direct simulations requires more realistic velocity profiles. Following Reynolds & Hussain (1972), we have used Cess (1958) approximate profiles for turbulent channels at $\delta^+ = 185$, 550, 950 and 2000. The resulting growth rates and phase velocities are portrayed in figures 18(*a*) and 18(*b*) for different values of L_w. The results for the different Reynolds numbers are virtually indistinguishable when expressed in wall units, except perhaps for the $\delta^+ = 185$ case, for which the Cess approximation is less accurate. This is consistent with the hypothesis in § 5.2 that the wavelength of the spanwise rollers scales in wall units. Figure 18(*c*) shows a sharp transition in the flow stability for

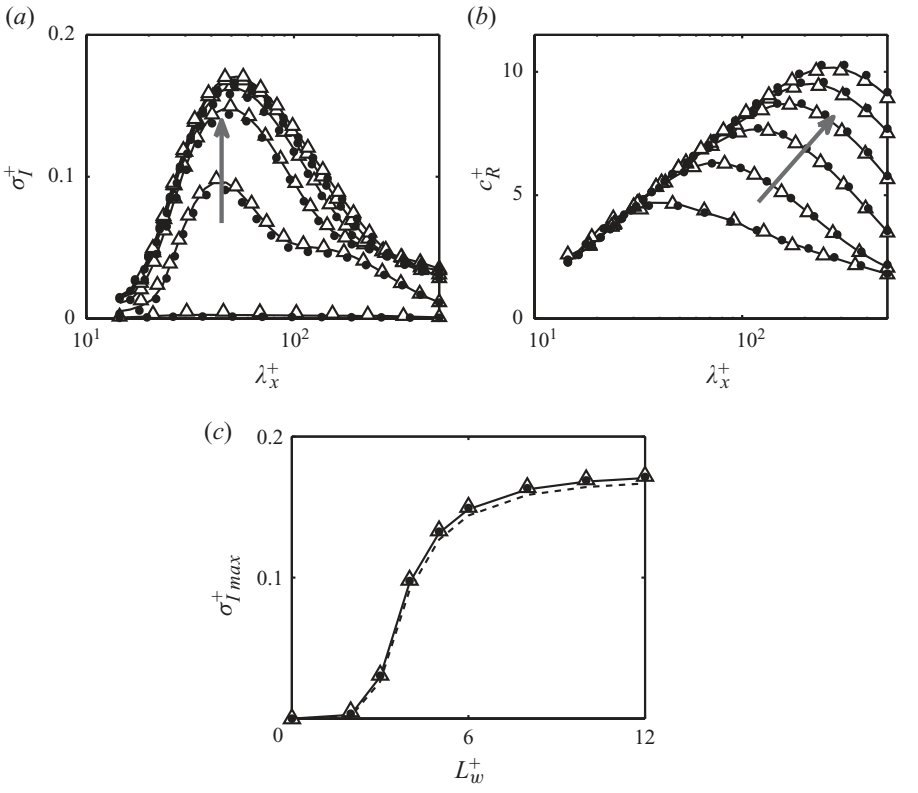

FIGURE 18. (*a*) Growth rate $\sigma_I^+ = \alpha^+ \mathrm{Im}(c^+)$ of the unstable modes of turbulent profiles with the boundary condition of (6.11). (*b*) Corresponding phase velocity, $\mathrm{Re}(c^+) = c_R^+$. ●, $\delta^+ = 185$; ——, 550; △, 2000. Curves are shown for $L_w^+ = 2(2)12$, with arrows indicating increasing L_w^+. (*c*) Maximum growth rate as a function of L_w^+: – – – –, $\delta^+ = 185$; ——, 550; ●, 950; △, 2000.

$L_w^+ \approx 4$, below which the eigenmodes are quasi-neutral, and above which the maximum growth rate is nearly constant. Using the approximate relation (6.13), this transition roughly corresponds to $\ell_g^+ \approx 11$, which is close to the limit found in § 3 for the breakdown of the viscous regime in the riblet experiments. The empirical collapse for ℓ_g^+ can thus be explained by the theoretical model for the instability, with the breakdown actually corresponding to the onset of the instability at $L_w^+ \approx 4$.

The growth rate and phase velocity curves of figure 18 are qualitatively similar to those for the piecewise-linear profile in figure 17, except for the shortest streamwise wavelengths at the largest L_w^+, which are stable in the piecewise-linear case and weakly unstable in the channels. The reason is probably that those wavelengths are too short in the piecewise-linear case to interact with the singularity at $y = H$ of the profile of U'', which is the key energy-producing term in the Rayleigh equation (6.3). In the turbulent channels, U'' is non-zero everywhere.

On the other hand, the similarity of the eigenvalues for longer wavelengths suggests that the channels behave approximately as a piecewise-linear profile in which $H^+ \approx 10$. That is interesting because it is slightly surprising that an instability derived from the inviscid Rayleigh equation should scale in viscous wall units. In fact, wall units are not only a measure of the Reynolds number of the perturbations, but they also encode the shape of the mean profile. Specifically, the energy-producing term, U'', has

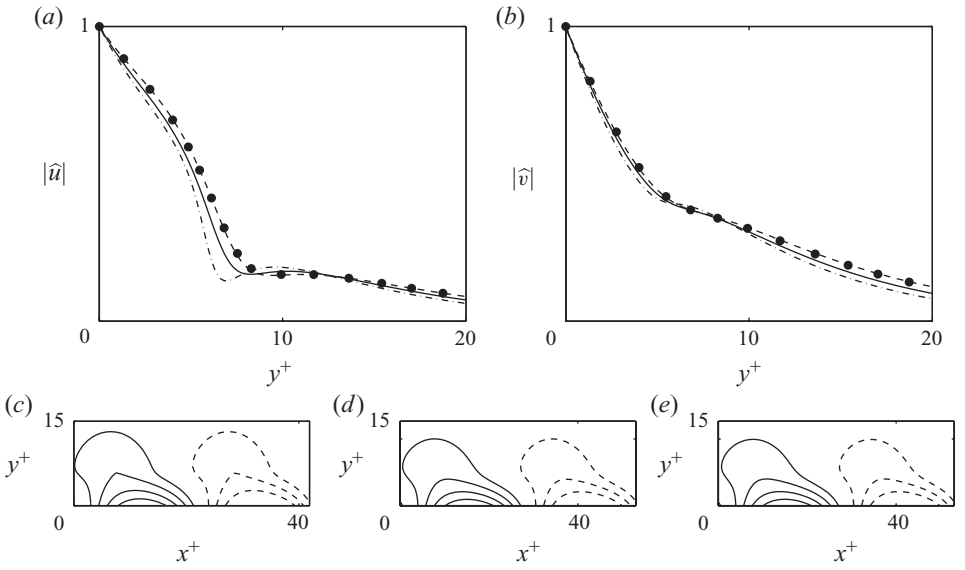

FIGURE 19. (*a*) $|\widehat{u}|$ and (*b*) $|\widehat{v}|$ profiles of the most amplified modes for a turbulent channel profile with $\delta^+ = 550$. – · – , $L_w^+ = 4$; ——, 6; – – – –, 8; ●, 14. (*c–e*) *u–v* perturbation streamlines of those modes for (*c*) $L_w^+ = 4$, (*d*) 8 and (*e*) 14. The solid lines correspond to clockwise rotation.

a fairly sharp maximum between $y^+ = 5$ and 20 in channels, peaking near $y^+ = 7$, which plays the same role as the singularity at $y = H$ of the piecewise-linear profile. That peak scales in wall units and, in all probability, is responsible for the wall scaling of the observed instability.

The most amplified modes for L_w^+ in the range of the onset of strong instability are portrayed in figure 19 for $\delta^+ = 550$ and are practically identical for the other Reynolds numbers. The rollers have heights of $y^+ \approx 15$, which agree well with the observations from our DNSs, and convection velocities $\mathrm{Re}(c^+) \approx 6$, which are also in reasonable agreement with the observed $U_C^+ \approx 6$–8. Figure 19(*c*) shows how the perturbations penetrate below $y = 0$, as some of the DNS rollers of figure 14 do. On the other hand, the predicted streamwise wavelengths are twice shorter than the observed $\lambda_x^+ \approx 150$, probably because viscosity, which is absent in the model, damps the shorter wavelengths in the channel, shifting the maximum amplification towards longer waves.

7. Conclusions

We have reviewed the regimes for drag reduction in ribbed surfaces, centring on the nature of the viscous breakdown in which the linear behaviour of the drag reduction with the riblet size ceases to apply. This is the limit that determines the optimal performance of a given riblet geometry. We have shown that the effect of the riblet size is better characterized by the square root of the groove cross-section, $\ell_g^+ = (A_g^+)^{1/2}$, than by other geometric parameters. In the experiments reviewed, spanning the full range of 'classical' riblets, the optimum is achieved for $\ell_g^+ \approx 10.7$, with a scatter of about 10 %. That value can be used to predict the maximum drag reduction as $DR_{max} \approx 0.83 \times 10.7 \times m_\ell$ with an error below 20 %, requiring only the value of the

slope of the drag curve in the viscous regime, obtainable from two-dimensional Stokes computations.

We have analysed the relationship between performance and riblet size from direct numerical simulations spanning the whole range of riblet behaviours, from drag reduction to drag increase. We have shown that the overlying quasi-streamwise vortices of the turbulent buffer layer tend to get localized above the riblet grooves, but that the vortices do not appear to lodge within the groove over the whole range of our simulations. Contrary to some previous conjectures, this vortex localization does not appear to be involved in the drag-reduction mechanism because it is relatively weak for the riblets that reduce drag and only becomes strong beyond the viscous breakdown. We have found that the breakdown coincides with the disappearance of a transverse recirculating region in the riblet grooves, which weakens and becomes increasingly asymmetric beyond the observed breakdown of the viscous regime. That coincides with the increase of the Reynolds stresses measured at the plane of the riblet tips, that eventually leads to the degradation of the drag.

On the other hand, the changes of the crossflow do not modify the streamwise flow within the grooves substantially, and the slip velocity measured at the riblet tips follows the prediction of the viscous Stokes regime for the whole range of our simulations. The main change at the time of the breakdown is the appearance of essentially two-dimensional spanwise rollers just above the wall, $y^+ \lesssim 20$, with characteristic streamwise wavelengths $\lambda_x^+ \approx 150$. They are similar to those found over permeable and porous surfaces and canopies, and can be traced to a Kelvin–Helmholtz-like instability associated with the relaxation of the impermeability condition for the wall-normal velocity. The extra Reynolds stresses associated with those rollers account for most of the drag degradation observed past the breakdown of the viscous regime.

We have presented a simplified inviscid model for that instability which confirms its Kelvin–Helmholtz nature, and which agrees reasonably well with the observed wavelengths and shapes of the perturbation. The parameter that determines the onset of the instability is a penetration length L_w^+ that, for conventional riblet geometries, is essentially proportional to the empirical parameter ℓ_g^+ found above to characterize the breakdown. The instability turns on for $L_w^+ \gtrsim 4$, which corresponds to the empirical viscous breakdown point $\ell_g^+ \approx 11$. Although it might be surprising that an inviscid instability scales in viscous wall units, this is due to the scaling in wall units of the mean velocity profile near the wall.

This work was supported in part by the CICYT grant TRA2009-11498 and by the sixth framework AVERT program of the European Commission, AST5-CT-2006-030914. R.G.-M. was supported by an FPI fellowship from the Spanish Ministry of Education and Science.

REFERENCES

del Álamo, J. C. & Jiménez, J. 2009 Estimation of turbulent convection velocities and corrections to Taylor's approximation. *J. Fluid Mech.* **640**, 5–26.

Bechert, D. W. & Bartenwerfer, M. 1989 The viscous flow on surfaces with longitudinal ribs. *J. Fluid Mech.* **206**, 105–129.

Bechert, D. W., Bruse, M., Hage, W., van der Hoeven, J. G. T. & Hoppe, G. 1997 Experiments on drag-reducing surfaces and their optimization with adjustable geometry. *J. Fluid Mech.* **338**, 59–87.

Breugem, W. P., Boersma, B. J. & Uittenbogaard, R. E. 2006 The influence of wall permeability on turbulent channel flow. *J. Fluid Mech.* **562**, 35–72.

Bruse, M., Bechert, D. W., van der Hoeven, J. G. T., Hage, W. & Hoppe, G. 1993 Experiments with conventional and with novel adjustable drag-reducing surfaces. In *Near-Wall Turbulent Flows* (ed. R. M. C. So, C. G. Speziale & B. E. Launder), pp. 719–738. Elsevier.

Cess, R. D. 1958 A survey of the literature on heat transfer in turbulent tube flow. *Report* 8-0529-R24. Westinghouse Research.

Choi, H., Moin, P. & Kim, J. 1993 Direct numerical simulation of turbulent flow over riblets. *J. Fluid Mech.* **255**, 503–539.

Chu, D. C. & Karniadakis, G. E. M. 1993 A direct numerical simulation of laminar and turbulent flow over riblet-mounted surfaces. *J. Fluid Mech.* **250**, 1–42.

Clauser, F. H. 1956 The turbulent boundary layer. *Adv. Appl. Mech.* **4**, 1–51.

Drazin, P. G. & Reid, W. H. 1981 *Hydrodynamic Stability*. Cambridge University Press.

El-Samni, O. A., Chun, H. H. & Yoon, H. S. 2007 Drag reduction of turbulent flow over thin rectangular riblets. *Intl J. Engng Sci.* **45**, 436–454.

Fadlun, E. A., Verzicco, R., Orlandi, P. & Mohd-Yusof, J. 2000 Combined immersed-boundary finite-difference methods for three-dimensional complex flow simulations. *J. Comput. Phys.* **161**, 35–60.

Ferziger, J. H. & Perić, M. 1996 *Computational Methods for Fluid Dynamics*. Springer.

Finnigan, J. 2000 Turbulence in plant canopies. *Annu. Rev. Fluid Mech.* **32**, 519–571.

García-Mayoral, R. & Jiménez, J. 2007 On the effect of riblet geometry on drag reduction. *Tech. Rep.* ETSIA/MF-072. School of Aeronautics, Universidad Politécnica de Madrid.

García-Mayoral, R. & Jiménez, J. 2011 Drag reduction by riblets. *Phil. Trans. R. Soc.* A **369**, 1412–1427.

Goldstein, D. B., Handler, R. & Sirovich, L. 1995 Direct numerical simulation of turbulent flow over a modeled riblet covered surface. *J. Fluid Mech.* **302**, 333–376.

Goldstein, D. B. & Tuan, T. C. 1998 Secondary flow induced by riblets. *J. Fluid Mech.* **363**, 115–151.

Hoyas, S. & Jiménez, J. 2008 Reynolds number effects on the Reynolds-stress budgets in turbulent channels. *Phys. Fluids* **20**, 101511.

Iaccarino, G. & Verzicco, R. 2003 Immersed boundary technique for turbulent flow simulations. *Appl. Mech. Rev.* **56** (3), 331–347.

Itoh, M., Tamano, S., Iguchi, R., Yokota, K., Akino, N., Hino, R. & Kubo, S. 2006 Turbulent drag reduction by the seal fur surface. *Phys. Fluids* **18** (6), 065102.

Jiménez, J. 1992 Wall friction and the structure of near-wall turbulence. In *11th Australasian Fluid Mech. Conf.* (ed. M. R. Davis & G. J. Walker), pp. 813–816. Hobart, Australia.

Jiménez, J. 1994 On the structure and control of near wall turbulence. *Phys. Fluids* **6** (2), 944–953.

Jiménez, J. 2004 Turbulent flows over rough walls. *Annu. Rev. Fluid Mech.* **36**, 173–196.

Jiménez, J. & Pinelli, A. 1999 The autonomous cycle of near wall turbulence. *J. Fluid Mech.* **389**, 335–359.

Jiménez, J., Uhlman, M., Pinelli, A. & Kawahara, G. 2001 Turbulent shear flow over active and passive porous surfaces. *J. Fluid Mech.* **442**, 89–117.

Jung, W. J., Mangiavacchi, N. & Akhavan, R. 1992 Suppression of turbulence in wall-bounded flows by high-frequency spanwise oscillations. *Phys. Fluids* A **4**, 1605–1607.

Kim, J., Moin, P. & Moser, R. D. 1987 Turbulence statistics in fully developed channel flow at low Reynolds number. *J. Fluid Mech.* **177**, 133–166.

Le, H. & Moin, P. 1991 An improvement of fractional step methods for the incompressible Navier–Stokes equations. *J. Comput. Phys.* **92** (2), 369–379.

Lee, S.-J. & Lee, S.-H. 2001 Flow field analysis of a turbulent boundary layer over a riblet surface. *Exp. Fluids* **30**, 153–166.

Linnick, M. N. & Fasel, H. F. 2005 A high-order immersed interface method for simulating unsteady incompressible flows on irregular domains. *J. Comput. Phys.* **204** (1), 157–192.

Luchini, P. 1995 Asymptotic analysis of laminar boundary-layer flow over finely grooved surfaces. *Eur. J. Mech.* B/*Fluids* **14**, 169–195.

Luchini, P., Manzo, F. & Pozzi, A. 1991 Resistance of a grooved surface to parallel flow and cross-flow. *J. Fluid Mech.* **228**, 87–109.

Nördstrom, J., Mattsson, K. & Swanson, C. 2007 Boundary conditions for a divergence free velocity-pressure formulation of the Navier–Stokes equations. *J. Comput. Phys.* **225**, 874–890.

Orlandi, P. & Jiménez, J. 1994 On the generation of turbulent wall friction. *Phys. Fluids* **6**, 634–641.

Orlandi, P., Leonardi, S. & Antonia, R. A. 2006 Turbulent channel flow with either transverse or longitudinal roughness elements on one wall. *J. Fluid Mech.* **561**, 279–305.

Py, C., de Langre, E. & Moulia, B. 2006 A frequency lock-in mechanism in the interaction between wind and crop canopies. *J. Fluid Mech.* **568**, 425–449.

Raupach, M. R., Finnigan, J. & Brunet, Y. 1996 Coherent eddies and turbulence in vegetation canopies: the mixing-layer analogy. *Boundary-Layer Meteorol.* **78**, 351–382.

Reynolds, W. C. & Hussain, A. K. M. F. 1972 The mechanics of an organized wave in turbulent shear flow. Part 3. Theoretical models and comparisons with experiments. *J. Fluid Mech.* **54**, 263–288.

Roshko, A. 1953 On the development of turbulent wakes from vortex streets. *NACA Tech. Note* 2913.

Simens, M. P., Jiménez, J., Hoyas, S. & Mizuno, Y. 2009 A high-resolution code for turbulent boundary layers. *J. Comput. Phys.* **228**, 4218–4231.

Stalio, E. & Nobile, E. 2003 Direct numerical simulation of heat transfer over riblets. *Intl J. Heat Fluid Flow* **24**, 356–371.

Suzuki, Y. & Kasagi, N. 1994 Turbulent drag reduction mechanism above a riblet surface. *AIAA J.* **32** (9), 1781–1790.

Tennekes, H. & Lumley, J. L. 1972 *A First Course in Turbulence*. MIT Press.

Walsh, M. J. 1990*a* Effect of detailed surface geometry on riblet drag reduction performance. *J. Aircraft* **27** (6), 572–573.

Walsh, M. J. 1990*b* Riblets. In *Viscous Drag Reduction in Boundary Layers* (ed. D. M. Bushnell & J. N. Hefner), pp. 203–261. AIAA.

Walsh, M. J. & Lindemann, A. M. 1984 Optimization and application of riblets for turbulent drag reduction. *AIAA Paper* 84-0347.

Williamson, C. H. K. 1989 Oblique and parallel modes of vortex shedding in the wake of a circular cylinder at low Reynolds numbers. *J. Fluid Mech.* **206**, 579–627.